Middle East Journal of Science

www.dergipark.org.tr/mejs

MEJS

VOLUME 9
ISSUE 1

JUNE
2023

E-ISSN
2618-6136

Email: bilgumus@gmail.com
Visit our home page on www.dergipark.org.tr/mejs

Tamraz H. TAMRAZOV
Field: Biological Sciences
(Assoc.Prof.Dr., Department of Plant Physiology and Biotechnology, Research Institute of Crop Husbandry, Ministry of Agriculture of the Republic of Azerbaijan)
tamraz.tamrazov@mail.ru

Yusuf ZEREN

Field: Mathematics, Topology

(Assoc.Prof.Dr., Yıldız Technical University, Faculty of Science and Letters, Dep. of Mathematics, TURKEY)

yzeren@yildiz.edu.tr

Z. Gökay KAYNAK

Field: Nuclear Physics

(Retired Prof.Dr., Uludag University, Faculty of Science, Dep. of Physics, Turkey) kaynak@uludag.edu.tr

Middle East Journal of Science

https://dergipark.org.tr/mejs

e-ISSN:2618-6136

MEJS
Volume 9
Issue 1
June 2023

CONTENTS

Research Articles

Middle East Journal of Science

https://dergipark.org.tr/mejs **MEJS**

e-ISSN:2618-6136

Research Article

AN EXTENSIVE STUDY ON MACRO-HETEROCERA (LEPIDOPTERA) FAUNA OF THE BOTAN VALLEY NATIONAL PARK, TURKIYE

Erdem SEVEN

Batman University, Faculty of Tourism, Department of Gastronomy and Culinary Arts, 72060, Batman, Turkey
Corresponding author; erdem.seven@batman.edu.tr

Abstract: *This paper presents a faunal list of Macro-Heterocera species from the Botan Valley National Park, which is Turkey's 45th national park, consisting of approximately 120 thousand acres and 29 kilometers in south-eastern Turkey, comprising the superfamilies Bombycoidea, Drepanoidea, Geometroidea, Lasiocampoidea, Noctuoidea. The area has scarcely been investigated before. This study contains the first comprehensive faunal list of macro-moths of the Botan Valley National Park. Totally 135 Lepidoptera species were determined. Among them, 99 moth species are newly reported from the Botan Valley National Park, and 6 of them are newly discovered in Siirt province. Examined samples and the location of each species are presented. Information on sites and collection dates are mentioned.*

Keywords*: Distribution, Fauna, Moth, The Botan Valley National Park, Türkiye*

Received: November 23, 2021 *Accepted: May 29, 2023*

1. Introduction

The Botan River is placed in hilly-rocky geography, and has an altitude between 470-1360 meters, consisting of limestone mountain and plateau formations [1]. The river originates from the Uluçay Stream in the south of Bitlis province. It is positioned at the intersection of Southeastern Anatolia and Eastern Anatolia Regions, and extends from east to south of Siirt province, joining the Tigris River. The Botan Stream surrounds the Norduz Plateau from the west and takes its source from the high mountains forming the borders of the Siirt-Hakkari and Siirt-Van provinces [2-3]. The Botan Valley National Park is located in Siirt province, hosting natural beauty within the borders of central Siirt, Tillo, and Eruh districts [4]. The Botan Valley is very curved and rotating and commonly consists of rocky mountainous areas (Figure 1). A rich ecosystem diversity has been created within the valley with the effect of the geomorphological structure. In the upper parts of the mountains, oak trees are common vegetation while the slopes of the mountains contain *Paliurus* and *Juniperus* plants. In addition, *Salix*, *Platanus*, *Junglans*, and *Tamarix* species are seen with rich herbaceous vegetation along the edge of the Botan River.

The Macro-Heterocera of Siirt province was well studied, especially the northern part and approximately 500 macro-moth records have been presented by Kemal et al. [6-7], Kemal & Seven [8-9], Seven [5, 10-14], Koçak & Kemal [15] and Seven et al. [16-17]. However, extensive research have not been carried out on the Botan Valley National Park. As a first step in investigating the region, a list of 83 noctuoid species from the area has been published by Seven [5]. The present paper evaluates macro-moths collected in 2015-2020 (excluding noctuoids in 2015-2016 [5]), and new records from the Botan Valley National Park and Siirt province are presented.

2. Materials and Methods

The materials were collected between the years 2015-2020 by irregular expeditions in 7 locations from the Botan Valley National Park, Siirt prov., south-eastern Turkey (Table 1). The previous study in 2019 [5] evaluated only the noctuoid species collected from the Botan Valley in 2015-2016, and was published as the first report. This paper includes noctuoid moths, which were captured afterward in 2017-2020; as well as other Macro-Heterocera families that were not examined in 2015-2016, and their specimens collected subsequently. A sweep net was used to capture the diurnal species and the nocturnal samples were caught with light traps which were formed of UV strip led, 12 volts and 7-ampere battery, a poison bottle with ethyl acetate, and a vowel box. The samples were identified after being pinned, labeled, and stretched. The specimens were diagnosed according to external characters and genital structures. The genital dissections were made with. ca 10% potassium hydroxide (KOH) to macerate the full abdomen. The cleaned abdominal segments and the genital organs were dehydrated in 96% ethanol before mounting in euparal. The materials were stored in the Batman University Entomology Research Laboratory (BTU). Terminology follows that of Seven [5], Koçak & Kemal [15], Seven et al. [17], Kornoşor [18-19], De Freina [20], Seven [21], Hausmann [22-23], Ronkay et al. [24], Mironov [25], Zilli, et al. [26], Leraut [27], Hausmann & Viidalepp [28], Lödl et al. [29], Skou & Sihvonen [30], Müller et al. [31], Lepiforum e. V. [32].

Table 1. Data on sites and collection dates

Site	Altitude	Coordinate	Collection Date	Habitat
Botan road, 12 km SW	700 m	37°52'29" N 41°53'07" E	25.04.2015, 09.07.2015, 10.08.2015, 07.09.2015, 24.05.2016, 10.10.2020, 18.11.2020	Rocky area
Botan road, 3 km SW	780 m	37°53'24" N 41°53'03" E	16.03.2018, 24.08.201916.09.2020,	Oak, *Paliurus*, *Amygdalus* field
Kale, Tillo	1300 m	37°57'08" N 42°01'58" E	22.07.2018, 11.03.2020	Steppe
Yerlibahçe	955 m	37°53'11" N 41°53'56" E	19.06.2017	Mountain steppe
Gökçebağ	750 m	37°51'27" N 41°52'34" E	23.03.2019, 15.04.2020	Oak field
Uluçay	555 m	37°51'26" N 41°53'09" E	12.08.2015, 28.10.2015, 21.08.2016	Rocky mountains
Sağlarca crossroad	465 m	37°49'14" N 41°51'59" E	20.05.2015, 28.03.2016, 20.10.2016	Riverside

Uluçay and Sağlarca locations, which were studied between 2015-2016, were submerged at the end of 2019 due to the rising waters of the Ilısu Dam. In the results section, newly identified species for Siirt province are marked with an asterisk (*). Previously reported 36 noctuoid moths in the paper of Seven [5] are indicated by a plus sign ($^{+}$). Species are presented alphabetically within their subfamilies.

Figure 1. The Botan Valley, Botan road, 12 km SW, 700 m, 19.11.2020

3. Results

Superfamily Noctuoidea Latreille, 1809

Family Erebidae Leach, [1815]

Subfamily Erebinae Leach, [1815]

***Aedia funesta* (Esper, [1766])** Material: Yerlibahçe, 955 m, 19.06.2017, ♂; Kale, Tillo, 1300 m, 22.07.2018, 2♂♂, 3♀♀.

Subfamily Toxocampinae Guenée, 1852

***Autophila banghaasi* Boursin, 1940** Material: Yerlibahçe, 955 m, 19.06.2017, ♀; Kale, Tillo, 1300 m, 22.07.2018, ♂.

Tathorhynchus exsiccata* (Lederer, 1855) Material: Botan road, 12 km SW, 700 m, 16.09.2020, ♂.

Subfamily Boletobiinae Guenée, [1858]

***Calymma communimacula* ([Denis & Schiffermüller], 1775)** Material: Yerlibahçe, 955 m, 19.06.2017, 2♂♂; Botan road, 12 km SW, 700 m, 16.09.2020, 2♂♂, ♀.

***Eublemma ostrina* (Hübner, [1808])**+ Material: Botan road, 12 km SW, 700 m, 10.10.2020, 4♂♂, 3♀♀; Botan road, 3 km SW, 24.08.2019, 2♂♂, 2♀♀.

***Eublemma parva* (Hübner, [1808])** Material: Kale, Tillo, 1300 m, 22.07.2018, 2♂♂, 3♀♀.

***Eublemma polygramma* (Duponchel, [1842])** Material: Kale, Tillo, 1300 m, 22.07.2018, 3♂♂, 2♀♀; Botan road, 3 km SW, 24.08.2019, ♂.

***Metachrostis dardouini* (Boisduval, 1840)** Material: Yerlibahçe, 955 m, 19.06.2017, ♂, ♀.

Subfamily Catocalinae Boisduval, 1828

***Catocala abacta* Staudinger, 1900** Material: Kale, Tillo, 1300 m, 22.07.2018, 4♂♂, 6♀♀; Yerlibahçe, 955 m, 19.06.2017, 2♂♂, 3♀♀; Botan road, 3 km SW, 24.08.2019, ♂.

***Catocala elocata* (Esper, [1787])** Material: Kale, Tillo, 1300 m, 22.07.2018, ♂; Botan road, 3 km SW, 24.08.2019, ♀.

***Catocala nymphagoga* (Esper, [1787])** Material: Yerlibahçe, 955 m, 19.06.2017, 2♂♂, ♀; Kale, Tillo, 1300 m, 22.07.2018, 2♂♂.

***Dysgonia algira* (Linnaeus, 1767)** Material: Yerlibahçe, 955 m, 19.06.2017, 2♂♂; Kale, Tillo, 1300 m, 22.07.2018, 2♂♂, 2♀♀; Botan road, 3 km SW, 24.08.2019, ♂.

***Grammodes stolida* (Fabricius, 1775)** + Material: Kale, Tillo, 1300 m, 22.07.2018, ♂, 2♀♀; Botan road, 3 km SW, 24.08.2019, 2♂♂, ♀; Botan road, 12 km SW, 700 m, 16.09.2020, ♂, 10.10.2020, ♂.

***Minucia lunaris* ([Denis & Schiffermüller], 1775)** Material: Gökçebağ, 750 m, 15.04.2020, 2♂♂.

***Pericyma albidentaria* (Freyer, [1841])** + Material: Yerlibahçe, 955 m, 19.06.2017, 3♂♂, 2♀♀; Kale, Tillo, 1300 m, 22.07.2018, ♂; Botan road, 12 km SW, 700 m, 10.10.2020, ♂.

Subfamily Hypeninae Herrich-Schäffer, [1851]

***Hypena munitalis* Mann, 1861**+ Material: ♂; Botan road, 12 km SW, 700 m, 16.09.2020, ♂.

***Zekelita ravalis* (Herrich-Schäffer, [1852])**+ Material: Yerlibahçe, 955 m, 19.06.2017, 3♂♂, 2♀♀; Botan road, 12 km SW, 700 m, 16.09.2020, 2♂♂.

***Zethes brandti* Janzon, 1977** Material: Kale, Tillo, 1300 m, 22.07.2018, ♂; Botan road, 12 km SW, 700 m, 16.09.2020, ♂.

Subfamily Herminiinae Leach, [1815]

***Idia calvaria* ([Denis & Schiffermüller], 1775)** Material: Kale, Tillo, 1300 m, 22.07.2018, 2♂♂.

Subfamily Anobinae Holloway, 2005

***Plecoptera inquinata* (Lederer, 1857)** + Material: Yerlibahçe, 955 m, 19.06.2017, 3♂♂, 2♀♀; Kale, Tillo, 1300 m, 22.07.2018, 2♂♂; Botan road, 12 km SW, 700 m, 16.09.2020, 2♂♂, ♀.

Subfamily Arctiinae Leach, [1815]

***Cymbalophora oertzeni* (Lederer, 1855)** Material: Botan road 12 km SW, 700 m, 10.10.2020, 2♂♂; Sağlarca crossroad, 465 m, 20.10.2016, ♂.

***Dysauxes famula* (Freyer, 1836)** Material: Botan road 12 km SW, 700 m, 16.09.2020, ♂, ♀; 10.10.2020, 3♂♂.

***Utetheisa pulchella* (Linnaeus, 1758)** Material: Kale, Tillo, 1300 m, 22.07.2018, 2♂♂, 3♀♀; Botan road 12 km SW, 700 m, 16.09.2020, ♂.

***Ocnogyna loewii* (Zeller, 1846)** Material: Botan road 12 km SW, 700 m, 18.11.2020, ♂; Uluçay, 555 m, 28.10.2015, ♂.

***Paidia rica* (Freyer, [1855])** Material: Botan road, 3 km SW, 780 m, 24.08.2019, 2♂♂, 3♀♀; Kale, Tillo, 1300 m, 22.07.2018, 2♀♀; Yerlibahçe, 955 m, 19.06.2017, ♂.

Subfamily Lymantriinae Hampson, 1893

***Euproctis melania* (Staudinger, 1892)** Material: Uluçay, 555 m, 12.08.2015, ♂, 21.08.2016, ♂; Kale, Tillo, 1300 m, 22.07.2018, ♂.

***Leucoma salicis* (Linnaeus, 1758)** Material: Botan road, 12 km SW, 700 m, 16.09.2020, ♂, 10.10.2020, ♂.

***Leucoma Wiltshire* Collenette, 1938** Material: Uluçay, 555 m, 21.08.2016, 3♂♂; Botan road, 12 km SW, 700 m, 07.09.2015, ♂.

***Polymona lapidicola* (Herrich-Schäffer, [1852])** Material: Botan road, 12 km SW, 700 m, 16.09.2020, ♂, 10.10.2020, ♂.

Family Noctuidae Latreille, 1809

Subfamily Acontiinae Guenée, 1841

***Acontia trabealis* (Scopoli, 1763)** Material: Yerlibahçe, 955 m, 19.06.2017, 2♂♂, 2♀♀; Kale, Tillo, 1300 m, 22.07.2018, ♂; Botan road, 3 km SW, 24.08.2019, 2♂♂.

Subfamily Acronictinae Harris, 1841

***Acronicta aceris* (Linnaeus, 1758)** Material: Kale, Tillo, 1300 m, 22.07.2018, 2♂♂, ♀; Botan road, 3 km SW, 24.08.2019, ♀.

Subfamily Metoponiinae Herrich-Schäffer, 1851

***Aegle semicana* (Esper, [1798])** Material: Kale, Tillo, 1300 m, 22.07.2018, 2♂♂; Botan road, 3 km SW, 24.08.2019, ♀.

***Tyta luctuosa* ([Denis & Schiffermüller], 1775)**[+] Material: Kale, Tillo, 1300 m, 22.07.2018, 3♂♂; Botan road, 3 km SW, 24.08.2019, ♂.

Subfamily Psaphidinae Grote, 1896

***Allophyes renalis* (Wiltshire, 1941)** (Figure 2a) Material: Botan road, 12 km SW, 700 m, 18.11.2020, 2♂♂.

***Valeria oleagina* (Esper, [1786])** Material: Botan road, 3 km SW, 16.03.2018, ♂; Gökçebağ, 750 m, 23.03.2019, ♂.

Subfamily Plusiinae Boisduval, 1829

Abrostola agnorista* Dufay, 1956 Material: Botan road, 12 km SW, 700 m, 16.09.2020, ♂.

***Autographa gamma* (Linnaeus, 1758)**+ Material: Yerlibahçe, 955 m, 19.06.2017, 7♂♂, 2♀♀; Kale, Tillo, 1300 m, 22.07.2018, 3♂♂, 2♀♀; Botan road, 3 km SW, 24.08.2019, 4♂♂, 6♀♀.

***Trichoplusia ni* (Hübner, [1803])**+ Material: Yerlibahçe, 955 m, 19.06.2017, 5♂♂; Kale, Tillo, 1300 m, 22.07.2018, 3♂♂, 2♀♀; Botan road, 3 km SW, 24.08.2019, ♂.

Subfamily Xyleninae Guenée, 1852

***Agrochola mansueta* (Herrich-Schäffer, [1850])** Material: Botan road, 12 km SW, 700 m, 10.10.2020, 3♂♂, ♀.

***Anthracia eriopoda* (Herrich-Schäffer, [1851])** Material: Botan road, 12 km SW, 700 m, 16.09.2020, ♀.

***Apamea polyglypha* (Staudinger, 1892)**+ Material: Yerlibahçe, 955 m, 19.06.2017, 2♂♂, ♀.

***Aporophyla australis* (Boisduval, 1829)**+ Material: Botan road, 12 km SW, 700 m, 18.11.2020, 5♂♂, 3♀♀.

***Aporophyla canescens* (Duponchel, [1827])** Material: Botan road, 12 km SW, 700 m, 10.10.2020, 5♂♂, ♀.

***Aporophyla nigra* (Haworth, [1809])** Material: Botan road, 12 km SW, 700 m, 18.11.2020, 3♂♂.

***Caradrina clavipalpis* (Scopoli, 1763)**+ Material: Yerlibahçe, 955 m, 19.06.2017, 4♂♂, 6♀♀; Kale, Tillo, 1300 m, 22.07.2018, 3♂♂; Botan road, 3 km SW, 24.08.2019, ♂; Botan road, 12 km SW, 700 m, 16.09.2020, ♀.

***Caradrina flavirena* (Guenée, 1852)**+ Material: Kale, Tillo, 1300 m, 22.07.2018, ♂, 2♀♀; Botan road, 12 km SW, 700 m, 10.10.2020, 2♂♂.

***Caradrina gilva* (Donzel, 1837)**+ Material: Yerlibahçe, 955 m, 19.06.2017, 2♂♂; Kale, Tillo, 1300 m, 22.07.2018, ♂.

Caradrina syriaca* (Staudinger, 1892) Material: Botan road, 12 km SW, 700 m, 10.10.2020, ♂, ♀.

***Episema korsakovi* (Christoph, 1885)**+ Material: Botan road, 12 km SW, 700 m, 10.10.2020, ♂.

***Episema tersa* ([Denis & Schiffermüller], 1775)**+ (Figure 2b) Material: Botan road, 12 km SW, 700 m, 10.10.2020, 2♂♂, ♀.

***Mesogona acetosellae* (Goeze, 1781)** Material: Botan road, 12 km SW, 700 m, 10.10.2020, ♂.

***Olivenebula subsericata* (Herrich-Schäffer, 1861)** Material: Botan road, 12 km SW, 700 m, 10.10.2020, ♂.

***Polymixis manisadjiani* (Staudinger, 1881)** Material: Botan road, 12 km SW, 700 m, 18.11.2020, 3♂♂.

***Polymixis rufocincta* (Geyer, 1828)**+ Material: Botan road, 12 km SW, 700 m, 18.11.2020, 2♂♂, 2♀♀.

***Spodoptera exigua* (Hübner, [1808])**+ Material: Yerlibahçe, 955 m, 19.06.2017, 3♂♂, 2♀♀; Kale, Tillo, 1300 m, 22.07.2018, 7♂♂.

Subfamily Noctuinae Latreille, 1809

***Agrotis bigramma* (Esper, [1790])**[+] Material: Botan road, 12 km SW, 700 m, 10.10.2020, 4♂♂, 6♀♀; 18.11.2020, 2♂♂, ♀.

***Agrotis ipsilon* (Hufnagel, 1766)** [+] Material: Yerlibahçe, 955 m, 19.06.2017, 5♂♂, 4♀♀; Kale, Tillo, 1300 m, 22.07.2018, 2♂♂, 2♀♀; Botan road, 3 km SW, 24.08.2019, 2♂♂; Botan road, 12 km SW, 700 m, 16.09.2020, 3♂♂, ♀.

***Agrotis puta* (Hübner, [1803])** [+] Material: Botan road, 12 km SW, 700 m, 10.10.2020, 2♂♂, 2♀♀, 18.11.2020, 3♂♂, ♀.

***Agrotis segetum* ([Denis & Schiffermüller], 1775)** [+] Material: Yerlibahçe, 955 m, 19.06.2017, 3♂♂; Kale, Tillo, 1300 m, 22.07.2018, 2♂♂, 2♀♀; Botan Road, 3 km SW, 24.08.2019, 4♂♂, 6♀♀; Botan road, 12 km SW, 700 m, 16.09.2020, 2♀♀, 10.10.2020, 3♂♂, 2♀♀.

***Dichagyris erubescens* (Staudinger, 1892)** [+] Material: Yerlibahçe, 955 m, 19.06.2017, 4♂♂, 6♀♀; Botan road, 3 km SW, 24.08.2019, 4♂♂, 5♀♀.

***Dichagyris singularis* (Staudinger, 1877)**[+] Material: Botan road, 12 km SW, 700 m, 16.09.2020, 3♂♂, ♀.

***Eugnorisma pontica* (Staudinger, 1892)** Material: Botan road, 12 km SW, 700 m, 16.09.2020, ♂, 2♀♀.

***Euxoa obelisca* ([Denis & Schiffermüller], 1775)** Material: Yerlibahçe, 955 m, 19.06.2017, 2♂♂; Kale, Tillo, 1300 m, 22.07.2018, ♀.

***Noctua comes* (Hübner, [1813])** Material: Yerlibahçe, 955 m, 19.06.2017, 2♂♂, 2♀♀; Kale, Tillo, 1300 m, 22.07.2018, 2♂♂; Botan road, 3 km SW, 24.08.2019, 2♂♂; Botan road, 12 km SW, 700 m, 16.09.2020, 3♂♂, 10.10.2020, 4♂♂, 2♀♀.

***Noctua orbona* (Hufnagel, 1766)** [+] Material: Kale, Tillo, 1300 m, 22.07.2018, ♂, 2♀♀; Botan Road, 3 km SW, 24.08.2019, 4♂♂, 2♀♀; Botan Road, 12 km SW, 700 m, 10.10.2020, 5♂♂, ♀.

***Noctua pronuba* (Linnaeus, 1758)** [+] Material: Yerlibahçe, 955 m, 19.06.2017, 3♂♂, ♀; Botan Road, 3 km SW, 24.08.2019, 3♂♂, 2♀♀; Kale, Tillo, 1300 m, 22.07.2018, ♂, 2♀♀.

***Xestia cohaesa* (Herrich-Schäffer, [1849])** [+] Material: Botan Road, 12 km SW, 700 m, 10.10.2020, 3♂♂, 2♀♀.

***Xestia palaestinensis* (Kalchberg, [1898])**[+] Material: Botan road, 12 km SW, 700 m, 10.10.2020, 2♂♂, ♀.

***Xestia xanthographa* ([Denis & Schiffermüller], 1775)** Material: Botan road, 12 km SW, 700 m, 10.10.2020, ♂.

Subfamily Bryophilinae Guenée, 1852

***Bryophila maeonis* Lederer, 1865** Material: Kale, Tillo, 1300 m, 22.07.2018, 2♂♂, 2♀♀; Botan road, 12 km SW, 700 m, 16.09.2020, 3♂♂.

***Bryophila raptricula* ([Denis & Schiffermüller], 1775)** [+] Material: Kale, Tillo, 1300 m, 22.07.2018, 4♂♂, 3♀♀; Botan road, 3 km SW, 24.08.2019, 5♂♂, 2♀♀.

***Bryopsis amasina* (Draudt, 1931)** Material: Botan road, 3 km SW, 24.08.2019, 2♂♂.

***Cryphia receptricula* (Hübner, [1803])** Material: Kale, Tillo, 1300 m, 22.07.2018, 3♂♂, ♀; Botan road, 3 km SW, 24.08.2019, 2♂♂, 2♀♀; Botan road, 12 km SW, 700 m, 16.09.2020, ♀.

***Cryphia tephrocharis* Boursin, 1954** Material: Botan road, 3 km SW, 24.08.2019, 4♂♂; Botan road, 12 km SW, 700 m, 16.09.2020, 2♂♂, 10.10.2020, ♂, 3♀♀.

***Victrix hackeri* Varga & Ronkay, 1991** Material: Botan road, 12 km SW, 700 m, 16.09.2020, 2♂♂.

Subfamily Hadeninae Guenée, 1837

***Hadena sancta* (Staudinger, 1859)** Material: Yerlibahçe, 955 m, 19.06.2017, ♂; Kale, Tillo, 1300 m, 22.07.2018, ♂.

***Leucania punctosa* (Treitschke, 1825)** + Material: Botan road, 12 km SW, 700 m, 16.09.2020, ♂, 10.10.2020, 3♂♂, 2♀♀.

***Mythimna alopecuri* (Boisduval, 1840)** + Material: Botan road, 12 km SW, 700 m, 16.09.2020, 2♂♂, 2♀♀, 10.10.2020, 3♂♂, 2♀♀.

***Mythimna l-album* (Linnaeus, 1767)** + Material: Yerlibahçe, 955 m, 19.06.2017, 4♂♂, 3♀♀; Kale, Tillo, 1300 m, 22.07.2018, ♂; Botan road, 12 km SW, 700 m, 10.10.2020, 3♂♂.

***Mythimna vitellina* (Hübner, [1808])** + Material: Yerlibahçe, 955 m, 19.06.2017, 2♂♂, 3♀♀; Kale, Tillo, 1300 m, 22.07.2018, 3♂♂, 2♀♀; Botan road, 3 km SW, 24.08.2019, 2♀♀; Botan road, 12 km SW, 700 m, 10.10.2020, 3♂♂.

Subfamily Oncocnemidinae Forbes & Franclemont, 1954

***Hypeuthina fulgurita* Lederer, 1855**+ Material: Botan road, 12 km SW, 700 m, 10.10.2020, 3♂♂, ♀.

***Oncocnemis fuscopicta* Wiltshire, 1976** Material: Botan road, 12 km SW, 700 m, 10.10.2020, 2♂♂, ♀.

***Stilbina hypaenides* Staudinger, 1892**+ Material: Botan road, 12 km SW, 700 m, 10.10.2020, 4♂♂, 2♀♀.

Family Nolidae Bruand, 1847

Subfamily Chloephorinae Stainton, 1859

***Arcyophora dentula* (Lederer, 1869)** Material: Botan road, 12 km SW, 700 m, 16.09.2020, ♂.

***Earias insulana* (Boisduval, 1833)** + Material: Yerlibahçe, 955 m, 19.06.2017, 2♂♂; Kale, Tillo, 1300 m, 22.07.2018, ♀.

Family Euteliidae Grote, 1882

Subfamily Euteliinae Grote, 1882

***Eutelia adulatrix* (Hübner, [1813])** Material: Gökçebağ, 750 m, 15.04.2020, ♂.

Family Thaumetopoeidae Aurivillius, 1891

Subfamily Thaumetopoeinae Aurivillius, 1889

***Thaumetopoea solitaria* (Freyer, [1838])** Material: Sağlarca crossroad, 20.10.2016, ♂; Botan road, 12 km SW, 700 m, 16.09.2020, ♂, 10.10.2020, ♂.

Family Notodontidae Stephens, 1829

Subfamily Phalerinae Butler, 1886

***Phalera bucephaloides* (Ochsenheimer, 1810)** Material: Botan road, 12 km SW, 700 m, 16.09.2020, 2♂♂.

Superfamily Drepanoidea Boisduval, 1828

Family Drepanidae Boisduval, 1828

Subfamily Drepaninae Boisduval, 1828

***Watsonalla binaria* (Hufnagel, 1767)** Material: Botan road, 3 km SW, 780 m, 24.08.2019, ♂.

Superfamily Lasiocampoidea Harris, 1841

Family Lasiocampidae Harris, 1841

Subfamily Lasiocampinae Harris, 1841

***Lasiocampa eversmanni* (Kindermann, 1843)** Material: Botan road, 12 km SW, 700 m, 10.10.2020, 2♂♂.

***Lasiocampa grandis* (Rogenhofer, 1891)** Material: Botan road, 12 km SW, 700 m, 10.10.2020, 3♂♂.

Superfamily Bombycoidea Latreille, 1802

Family Sphingidae Latreille, [1802]

Subfamily Smerinthinae Grote & Robinson, 1865

***Akbesia davidi* (Oberthür, 1884)** Material: Uluçay, 555 m, 12.08.2015, ♂.

***Marumba quercus* ([Denis & Schiffermüller], 1775** Material: Sağlarca crossroad, 20.10.2016, ♂; Botan road, 12 km SW, 700 m, 16.09.2020, ♀.

Subfamily Macroglossinae Harris, 1839

***Hyles livornica* (Esper, [1780])** Material: Yerlibahçe, 955 m, 19.06.2017, ♂; Kale, Tillo, 1300 m, 22.07.2018, ♂.

Superfamily Geometroidea Leach, 1815

Family Geometridae Leach, 1815

Subfamily Geometrinae Leach, 1815

***Aplasta ononaria* Fuessly, 1783** Material: Botan road, 12 km SW 700 m, 10.08.2015, ♀; Kale, Tillo, 1300 m, 22.07.2018, ♂.

***Phaiogramma etruscaria* (Zeller, 1849)** Material: Botan road, 12 km SW, 700 m, 24.05.2016, 2♂♂; Yerlibahçe, 955 m, 19.06.2017, ♀; Kale, Tillo, 1300 m, 22.07.2018, 2♂♂.

Subfamily Larentiinae Duponchel, 1845

***Aplocera plagiata* (Linnaeus, 1758)** Material: Botan road, 12 km SW 700 m, 10.10.2020, ♂.

***Camptogramma bilineata* Linnaeus, 1758** Material: Yerlibahçe, 955 m, 19.06.2017, 5♂♂; Kale, Tillo, 1300 m, 22.07.2018, ♀; Botan road, 12 km SW 700 m, 10.10.2020, 2♂♂, ♀.

***Chesistege korbi* Bohatsch, 1910** Material: Uluçay, 555 m, 28.10.2015, 2♂♂; Sağlarca crossroad, 465 m, 20.10.2016, ♂; Botan road, 12 km SW 700 m, 10.10.2020, 5♂♂, 18.11.2020, ♂.

***Eupithecia breviculata* Donzel, 1837** Material: Botan road, 12 km SW, 700 m, 25.04.2015, 2♂♂; Sağlarca crossroad, 465 m, 20.05.2015, ♂.

***Eupithecia ericeata* Rambur, 1833** Material: Sağlarca crossroad, 465 m, 20.10.2016, 7♂♂, 3♀♀; Botan road, 12 km SW, 700 m, 18.11.2020, ♂.

***Eupithecia oblongata* Thunberg, 1784** Material: Botan road, 12 km SW, 700 m, 16.09.2020, ♀.

***Eupithecia schiefereri* Dietze, 1904** Material: Botan road, 12 km SW, 700 m, 24.05.2016, ♂; Gökçebağ, 750 m, 15.04.2020, ♀.

***Nebula senectaria* Herrich-Schäffer, [1852]** Material: Sağlarca crossroad, 465 m, 20.10.2016, 2♂♂; Botan road, 12 km SW, 700 m, 18.11.2020, 3♂♂, ♀.

***Orthonama obstipata* Fabricius, 1794** Material: Gökçebağ, 750 m, 15.04.2020, 2♂♂.

***Xanthorhoe inconsiderata* (Staudinger, 1892)** Material: Botan road, 12 km SW, 700 m, 18.11.2020, 2♂♂.

Subfamily Ennominae Duponchel, 1845

***Apochima flabellaria* (Heeger, 1838)** Material: Gökçebağ, 750 m, 23.03.2019, ♂.

***Aspitates ochrearia* Rossi, 1794** Material: Botan road, 12 km SW 700 m, 25.04.2015, ♂, ♀; 09.07.2015, ♂; Uluçay, 555 m, 12.08.2015, ♀.

***Biston achyra* Wehrli, 1936** Material: Gökçebağ, 750 m, 23.03.2019, ♂; Kale, Tillo, 1300 m, 11.03.2020, ♂.

***Charissa mutilata* (Staudinger, 1879)** Material: Botan road, 12 km SW 700 m, 25.04.2015, 2♂♂.

***Charissa staudingeri* (Wnukowsky, 1929) *** Material: Botan road, 12 km SW 700 m, 10.10.2020, 3♂♂, ♀.

***Charissa subtaurica* Wehrli, 1934** Material: Botan road, 12 km SW 700 m, 10.08.2015, 3♂♂, 2♀♀; Sağlarca crossroad, 465 m, 20.10.2016, ♂.

***Chiasmia aestimaria* Hübner, 1809** Material: Botan road, 12 km SW, 700 m, 09.07.2015, ♂; 10.08.2015, 2♂♂; Uluçay, 12.08.2015, ♂, 21.08.2016, ♀.

***Dasycorsa modesta* Staudinger, 1879** Material: Sağlarca crossroad, 465 m, 28.03.2016, 5♂♂; Botan road, 3 km SW, 16.03.2018, 2♂♂; Gökçebağ, 750 m, 23.03.2019, ♂; Kale, Tillo, 1300 m, 11.03.2020, ♂.

***Dyscia innocentaria* Christoph, 1885** Material: Gökçebağ, 750 m, 15.04.2020, 2♀♀; Botan road, 12 km SW, 700 m, 10.10.2020, 2♂♂.

***Eilicrinia cordiaria* Hübner, 1790** Material: Uluçay, 12.08.2015, 6♂♂, ♀, 21.08.2015, ♂; Botan road, 12 km SW, 700 m, 07.09.2015, ♀; Botan road, 3 km SW, 780 m, 24.08.2019, 2♂♂.

***Eumera hoeferi* Wehrli, 1934** Material: Botan road, 12 km SW, 700 m, 10.10.2020, 2♂♂, ♀.

***Gnopharmia irakensis* Wehrli, 1938** Material: Yerlibahçe, 955 m, 19.06.2017, 2♂♂; Kale, Tillo, 1300 m, 22.07.2018, ♂, 2♀♀.

Gnophos chorista* Wehrli, 1939 Material: Botan road, 12 km SW, 700 m, 16.09.2020, 2♂♂, 2♀♀.

***Gnophos pseudosnelleni* Rjabov, 1964** Material: Botan road, 12 km SW, 700 m, 10.10.2020, 2♂♂.

***Gnophos sartatus* Treitschke, 1827** Material: Uluçay, 555 m, 28.10.2015, ♂; Botan road, 12 km SW, 700 m, 16.09.2020, ♂.

***Gnophos sacrarius* Staudinger, [1895]** Material: Uluçay, 555 m, 28.10.2015, ♂; Botan road, 12 km SW, 700 m, 10.10.2020, ♀.

***Neognopharmia stevenaria* (Boisduval, 1840)** Material: Uluçay, 555 m, 21.08.2016, 2♂♂; Yerlibahçe, 955 m, 19.06.2017, 2♂; Kale, Tillo, 1300 m, 22.07.2018, ♀; Botan road 3 km SW, 780 m, 24.08.2019, ♂.

Nychiodes divergaria* Staudinger, 1892 Material: Botan road, 12 km SW, 700 m, 07.09.2015, 4♂♂, 6♀♀, 24.05.2016, 2♂♂, 16.09.2020, ♂; Yerlibahçe, 955 m, 19.06.2017, ♂; Kale, Tillo, 1300 m, 22.07.2018, ♀; Botan road 3 km SW, 780 m, 24.08.2019, ♀.

***Peribatodes rhomboidaria* [Denis & Schiffermüller], 1775** Material: Botan road, 12 km SW, 700 m, 10.08.2015, 2♀♀; Yerlibahçe, 955 m, 19.06.2017, ♂; Kale, Tillo, 1300 m, 22.07.2018, 2♂♂.

***Selidosema plumaria* [Denis & Schiffermüller], 1775** Material: Sağlarca crossroad, 465 m, 20.10.2016, ♂; Botan road, 12 km SW, 700 m, 16.09.2020, ♂.

Subfamily Desmobathrinae Meyrick, 1886

***Myinodes shohami* Hausmann, 1994** Material: Botan road, 12 km SW, 700 m, 25.04.2015, 3♂♂, 2♀♀; Gökçebağ, 23.03.2019, ♂; Kale, Tillo, 1300 m, 11.03.2020, ♂.

Subfamily Sterrhinae Meyrick, 1892

***Cyclophora punctaria* (Linnaeus, 1758)** Material: Botan road, 12 km SW, 700 m, 16.09.2020, ♀.

***Idaea ochrata* Scopoli, 1763** Material: Sağlarca crossroad, 465 m, 20.05.2015, ♂.

***Idaea subsericeata* (Haworth, [1809])** Material: Yerlibahçe, 955 m, 19.06.2017, ♂; Kale, Tillo, 1300 m, 22.07.2018, 2♂♂.

***Rhodometra sacraria* (Linnaeus, 1767)** Material: Kale, Tillo, 1300 m, 22.07.2018, 2♀♀; Botan road, 3 km SW, 24.08.2019, 2♂♂; Botan road, 12 km SW, 700 m, 16.09.2020, 9♂♂, 2♀♀, 10.10.2020, ♂.

***Rhodostrophia discopunctata* Amsel, 1935** Material: Botan road, 12 km SW, 700 m, 24.05.2016, 3♂♂, ♀.

***Scopula decorata* [Denis & Schiffermüller], 1775** Material: Botan road, 3 km SW, 780 m, 24.08.2019, ♂.

***Scopula marginepunctata* Goeze, 1781** Material: Botan road, 12 km SW, 700 m, 24.05.2016, 7♂♂, 3♀♀, 16.09.2020, ♂, 10.10.2020, ♂; Yerlibahçe, 955 m, 19.06.2017, ♂; Kale, Tillo, 1300 m, 22.07.2018, ♀; Botan road 3 km SW, 780 m, 24.08.2019, ♂, 2♀♀.

***Scopula submutata* Treitschke, 1828** Material: Kale, Tillo, 1300 m, 22.07.2018, 3♂♂, ♀; Botan road, 12 km SW, 700 m, 16.09.2020, 2♂♂.

Figure 2. a. *Allophyes renalis*, b. *Episema tersa*

4. Conclusion

This study includes the first comprehensive faunal list of the Botan Valley. In this research, Macro-Heterocera of the Botan Valley National Park are evaluated, and 135 moth species are examined in Noctuoidea, Drepanoidea, Lasiocampoidea, Bombycoidea, Geometroidea, superfamilies: Erebidae (29), Noctuidae (54), Nolidae (2), Euteliidae (1), Thaumetopoeidae (1), Notodontidae (1); Drepanidae (1); Lasiocampidae (2); Sphingidae (3); Geometridae (41). Ennominae (Geometridae), Xyleninae and Noctuinae (Noctuidae) are the most crowded groups respectively (Table 2).

Table 2. The number of species in systematic classification

Superfamily	Family	Subfamily	Species number
Noctuoidea	Erebidae	Erebinae	1
		Toxocampinae	2
		Boletobiinae	5
		Catocalinae	7
		Hypeninae	3
		Herminiinae	1
		Anobinae	1
		Arctiinae	5
		Lymantriinae	4
	Noctuidae	Acontiinae	1
		Acronictinae	1
		Metoponiinae	2
		Psaphidinae	2
		Plusiinae	3
		Xyleninae	17
		Noctuinae	14
		Bryophilinae	6
		Hadeninae	5
		Oncocnemidinae	3
	Nolidae	Chloephorinae	2
	Euteliidae	Euteliinae	1
	Thaumetopoeidae	Thaumetopoeinae	1
	Notodontidae	Phalerinae	1

Table 2. Continued

Superfamily	Family	Subfamily	Species number
Drepanoidea	Drepanidae	Drepaninae	1
Lasiocampoidea	Lasiocampidae	Lasiocampinae	2
Bombycoidea	Sphingidae	Smerinthinae	2
		Macroglossinae	1
Geometroidea	Geometridae	Geometrinae	2
		Larentiinae	10
		Ennominae	20
		Desmobathrinae	1
		Sterrhinae	8
		Total	**135**

One erebid, *Tathorhynchus exsiccatus* (Lederer, 1855); 2 noctuids, *Abrostola agnorista* Dufay, 1956, *Caradrina syriaca* (Staudinger, 1892); and 3 geometrid moth species, *Charissa staudingeri* (Wnukowsky, 1929), *Gnophos chorista* Wehrli, 1939; *Nychiodes divergaria* Staudinger, 1892 are newly discovered from Siirt province.

Eighty-three noctuoid moth species from the Botan Valley were previously presented [5]. In this study, 99 macro moths are added to the region and the total number has increased to 182 species.

The diurnal species determined in the area include *Camptogramma bilineata* Linnaeus, 1758 (Geometridae); *Agrotis ipsilon* (Hufnagel, 1766); *A. segetum* ([Denis & Schiffermüller], 1775); *Autographa gamma* (Linnaeus, 1758); *Trichoplusia ni* (Hübner, [1803]) (Noctuidae).

The Botan Valley has been among the protected natural areas since 2019. Although some research has begun in recent years, it is a long-term study that takes time to fully reveal the flora and fauna elements of the area. In this regard, this study makes contributions to the determination of the biodiversity richness of the Botan Valley National Park.

Ethical statement

The author declares that this document does not require ethics committee approval or any special permission. Our study does not cause any harm to the environment.

Conflict of interest

The author declares no potential conflicts of interest related to this article's research, authorship, and publication.

References

[1] Atalay, I., Mortan, K., *Türkiye Bölgesel Coğrafyası (Regional Geography of Turkey)*, Inkılap Kitapevi, Istanbul, 2006.

[2] Alkan, A., "An Analytical Approach to the Ecotourism Potential of Middle and Lower Botan Valley", *Current Perspectives in Social Sciences*, 22 (Special issue 1), 475-499, 2018.

[3] Yangın, S., Botan çayı (Uluçay) vadisinin (Siirt) florası (The flora of the Botan stream (Uluçay) valley (Siirt)), Master thesis, Dicle University Institute of Science, Diyarbakır, Turkey, 2001.

[4] Official Gazette of the Republic of Turkey, Siirt ili, merkez, Aydınlar ve Eruh ilçeleri sınırları içerisinde bulunan bazı alanın 'Botan Vadisi Milli Parkı' olarak belirlenmesi hakkında karar

(30859), Ankara: Presidency General Directorate of Law and Legislation, 15 August 2019, pp. 9, 2019.

[5] Seven, E., "An Investigation on the Noctuid Moths (Lepidoptera) of Botan Valley, Southeastern Turkey", *The Black Sea Journal of Sciences*, 9(2), 238-252, 2019.

[6] Kemal, M., Koçak, A.Ö., Seven, E., "Spring aspect of the nocturnal Lepidoptera fauna of Şirvan District (Siirt Province) (southeast Turkey)", *Cesa News*, 11, 1-6, 2008.

[7] Kemal, M., Koçak, A.Ö., Seven, E., "Calophasia lunula in southeast Turkey (Lepidoptera, Noctuidae)", *Cesa News*, 64, 4-6, 2011.

[8] Kemal, M., Seven, E., "List of the nocturnal Lepidoptera of Şirvan with new faunal records to Siirt Province and Turkey (S.E. Turkey)," *Cesa News* 13, 1-2, 2008.

[9] Kemal, M., Seven, E., "Studies on the fauna and ecology of the Geometridae (Lepidoptera) in Şirvan district (Siirt Province, SE Turkey)", *Priamus Supplement*, 29, 1-48, 2013.

[10] Seven, E., Eco-faunistic studies on the Macroheterocera species in Şirvan district of Siirt (Lepidoptera), Ph. D. Thesis, Yüzüncü Yıl University, Van, Turkey, 2014.

[11] Seven, E., Contribution to the Macroheterocera (Lepidoptera) fauna of Siirt Province, *23. National Biology Congress*, 5-9 September, Gaziantep, Turkey, p. 427, 2016.

[12] Seven, E., "Ramitia kufrana sp. n. A New Species from Turkey (Lepidoptera, Geometridae)", *Journal of the Kansas Entomological Society*, 88(4), 430-433, 2016.

[13] Seven, E., "A new record and three little-known Eupithecia Curtis species from Turkey (Lepidoptera: Geometridae)", *Turkish Journal of Zoology*, 41, 583-586, 2017.

[14] Seven, E., "Notes on Some Species of Gnophini (Ennominae, Geometridae, Lepidoptera) from Turkey, with New Records", *Journal of the Entomological Research Society*, 20(1), 53-58, 2018.

[15] Koçak, A.Ö., Kemal, M., "A synonymous and distributional list of the species of the Lepidoptera of Turkey", *Memoirs*, 8, 1-487, 2018.

[16] Seven, E., Kemal, M., Koçak, A.Ö., "On the occurrence of Idia calvaria meridiorientalis in Siirt Province of SE Turkey (Lepidoptera, Noctuidae)", *Cesa News*, 102, 13-15, 2015.

[17] Seven, E., Ronkay, L., Ronkay, G., "Description of a new species of Deltote Reichenbach, Leipzig, 1817 (Lepidoptera, Noctuidae, Eustrotiinae) from Turkey and Turkmenistan", *Zootaxa* 4576(1), 171-178, 2019.

[18] Kornoşor, S., "Noctuidae (Lepidoptera) species of Turkey and preliminary list on their distributions, I. Trifidae group", *Ç.U. Faculty of Arts and Sciences Yearbook*, 1-2, 74-95, 1982.

[19] Kornoşor, S., "Noctuidae (Lepidoptera) species of Turkey and preliminary list on their distributions, II. Quadrifidae group", *Ç.U. Faculty of Arts and Sciences Yearbook*, 1-2, 95-102, 1982.

[20] De Freina, J., Witt, T.J., *Die Bombyces und Sphinges der Westpalaearktis*, Band 1. München, 1987.

[21] Seven, S., "Studies on the fauna and the ecology of the Lepidoptera of Turkey- I", *Priamus* 8(1/2), 1-52, 1996.

[22] Hausmann, A., *The Geometrid Moths of Europe 1*, Apollo Books, Stentrup, 2001.

[23] Hausmann, A., *The Geometrid Moths of Europe 2*, Apollo Books, Stenstrup, 2004.

[24] Ronkay, L., Yela J.L., Hreblay, M., *Noctuidae Europaeae, vol. 5, Hadeninae II*, Entomological Press, Denmark, 2001.

[25] Mironov, V., *The Geometrid Moths of Europe 4*, Apollo Books, Stenstrup, 2003.

[26] Zilli, A., Ronkay, L., Fibiger, M., *Noctuidae Europaeae, vol. 8, Apemeini*, Entomological Press, Denmark, 2005.

[27] Leraut, P., *Moths of Europe. Volume 2, Geometrid moths*. N.A.P. ed., Verrières-le-Buisson, 2009.

[28] Hausmann, A., Viidalepp, J., *The Geometrid Moths of Europe 3*, Apollo Books, Stenstrup, 2012.

[29] Lödl, M., Gaal-Haszler, S., Jovanovic-Kruspel, S., Ronkay, G., Ronkay, L., Varga, Z., Fibigeriana, *The Vartian Collection. Part I. Noctuoidea*, Heterocera press, 2012.

[30] Skou, P., Sihvonen, P., *The geometrid moths of Europe 5*, Brill, Leiden, 2015.

[31] Müller, B., Erlacher, S., Hausmann, A., Rajaei, H., Sihvonen, P., Skou, P., *The Geometrid Moths of Europe 6*, Leiden, Brill, 2019.

[32] Lepiforum e.V., Bestimmung von Schmetterlingen und ihren Präimaginalstadien. https://lepiforum.org/, 2023.

Middle East Journal of Science

https://dergipark.org.tr/mejs **MEJS**

e-ISSN:2618-6136

Research Article

RELAXING MULTICURVES ON THE TWICE PUNCTURED MÖBIUS BAND

***Ferihe ATALAN*[1] *Abdullah BAYKAL*[2]* * S.Öykü YURTTAŞ*[3]**

[1] Department of Mathematics, Atilim University, Ankara, 06830, Türkiye
[2] Department of Mathematics, Dicle University, Diyarbakır, 21280, Türkiye
[3] Department of Mathematics, Dicle University, Diyarbakır, 21280, Türkiye
*Corresponding author: baykal@dicle.edu.tr

Abstract: *An efficient way to describe multicurves (homotopy classes of finitely many essential simple closed curves) in an n-punctured non-orientable surface $N_{g,n}$ $(g > 1, n \geq 1)$ of genus g with one boundary component is achieved by the generalized Dynnikov coordinate system. In the case where $g = 1$ where the surface is, therefore, an n-punctured Möbius band, the generalized Dynnikov coordinate system gives a one-to-one map between the set of multicurves in $N_{1,n}$ and the set $Z^{2n-1} \setminus \{0\}$. In this paper, we describe an algorithm for relaxing an arbitrary multicurve in $N_{1,2}$ making use of generalized Dynnikov coordinates and the action of the mapping class group of $N_{1,2}$ in terms of generalized Dynnikov coordinates.*

Keywords: *Generalized Dynnikov coordinates, Möbius band, Multicurves*

Received: May 01, 2023 *Accepted: June 19, 2023*

1. Introduction

Given a surface S, a simple closed curve in S is called essential if it is not parallel to a puncture or a boundary component. When S is non-orientable there are two types of essential simple closed curves in S. If a regular neighborhood of the curve is an annulus it is called 2-sided, and if it is a Möbius band it is called 1-sided. A multicurve in S is a disjoint union of finitely many essential simple closed curves in S up to homotopy.

A beautiful way to describe multicurves in $N_{g,n}$ $(g > 1, n \geq 1)$ is achieved by the generalized Dynnikov coordinate system [9, 10]. In the case where $g = 1$ where the surface is an n-punctured Möbius band, the generalized Dynnikov coordinate system gives a one-to-one map between the set of multicurves in $N_{1,n}$, and $Z^{2n-1} \setminus \{0\}$. Let $\mathcal{L}_{1,n}$ be the set of multicurves in $N_{1,n}$. In this paper we focus on a combinatorial problem regarding multicurves in $N_{1,2}$. The problem is to improve a relaxation algorithm for a multicurve $\mathcal{L} \in \mathcal{L}_{1,2}$. More precisely, we compute a mapping class f (isotopy class of a homeomorphism) of $N_{1,2}$ such that $f(\mathcal{L})$ is relaxed, a particular multicurve where each component is either the core curve of the Möbius band or a curve intersecting the horizontal diameter of $N_{1,2}$ exactly twice.

Section 2 serves as a background to the paper which contains a short introduction to the generalized Dynnikov coordinates and a description of the mapping class group MCG($N_{1,2}$). Section 3 provides the necessary tools for Section 4 where an algorithm to relax a multicurve $\mathcal{L} \in \mathcal{L}_{1,2}$ is given.

2. Preliminaries

2.1. Generalized Dynnikov Coordinates

Consider the standard model of the n–punctured Möbius band $N_{1,n}$ as illustrated in Figure 1 where the punctures and the crosscap are aligned in the horizontal diameter of $N_{1,n}$. Here the disk with a cross drawn within it represents the crosscap which is obtained by removing the interior of the disk and then identifying the antipodal points in the resulting boundary component.

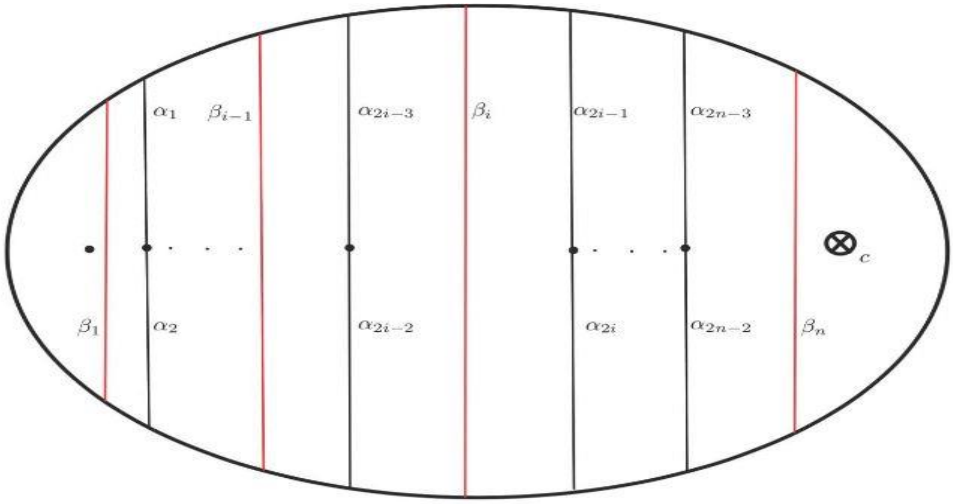

Figure 1. The core curve c and the arcs α_i, β_i on $N_{1,n}$

Consider the core curve c of the crosscap together with the arcs α_i $(1 \leq i \leq 2n-2)$ and β_i $(1 \leq i \leq n)$ depicted in Figure 1. Take a representative L of $\mathcal{L}$ intersecting the core curve and each of these arcs minimally. We call L a minimal representative of $\mathcal{L}$. For convenience, the number of intersections of L with the core curve c and each of the arcs α_i and β_i will also be denoted by the same symbols. We define the generalized Dynnikov coordinate function [9,10] ρ: $\mathcal{L}_{1,n} \rightarrow \mathrm{Z}^{2n-1} \setminus \{0\}$ by

$$\rho(\mathcal{L}) := (a; b; c) = (a_1, a_2, \dots a_{n-1}; b_1, b_2, \dots, b_{n-1}; c)$$

where

$$a_i = \frac{\alpha_{2i} - \alpha_{2i-1}}{2}, \qquad 1 \leq \mathrm{i} \leq \mathrm{n\text{-}1},$$

(1)

$$b_i = \frac{\beta_i - \beta_{i+1}}{2}, \qquad 1 \leq \mathrm{i} \leq \mathrm{n\text{-}1}$$

The vector $(\alpha; \beta; c) \in \mathrm{Z}^{3n-1} \setminus \{0\}$ therefore the multicurve $\mathcal{L}$) can be obtained from the generalized Dynnikov coordinates $(a; b; c) \in \mathrm{Z}^{2n-1} \setminus \{0\}$. Let

$$\beta_i^* = 2 \max_{1 \leq r \leq n-1} \left\{ |a_r| + \max(b_{r,0}) + \sum_{j=1}^{r-1} b_j \right\} - 2 \sum_{j=1}^{i-1} b_j$$

$$R = \max(0, c - \beta_n^* /2)$$

Then,

(2) $$\beta_i = \beta_i^* + 2R$$

$$\alpha_i = \begin{cases} (-1)^i a_{\lceil i/2 \rceil} + \dfrac{\beta_{\lceil i/2 \rceil}}{2} & \text{if } b_{\lceil i/2 \rceil} \geq 0, \\ (-1)^i a_{\lceil i/2 \rceil} + \dfrac{\beta_{1+\lceil i/2 \rceil}}{2} & \text{if } b_{\lceil i/2 \rceil} \leq 0, \end{cases} \quad (3)$$

where $\lceil x \rceil$ denotes the smallest integer which is not smaller than the value x.

This paper focuses on the case where $n = 2$. Therefore, the generalized Dynnikov coordinates of a multicurve $\mathcal{L}$ are given by the vector $(a; b; c) \in \mathbb{Z}^3 \backslash \{0\}$ where $(\alpha; \beta; c) \in \mathbb{Z}^5 \backslash \{0\}$ can be obtained by the above formula. Remark 2.1 points out the geometric interpretation of the parameter R.

Remark 2.1. Observe that for any essential simple closed curve except for such as those depicted in Figure 2, we have either $\alpha_1 - b \neq 0$ or $\alpha_2 - b \neq 0$ otherwise, there would be curves parallel to the boundary component. The parameter R counts the number of arcs of such curves which intersect α_1, α_2, and c exactly once.

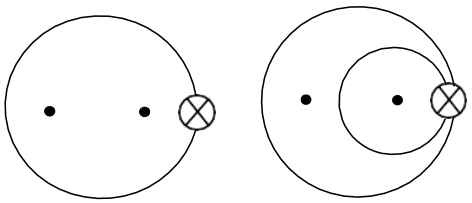

Figure 2. Geometric interpretation of the parameter R

2.2. Generators of MCG($N_{1,n}$)

The mapping class group MCG(S) of a given surface S is the group of isotopy classes of homeomorphisms of S (homeomorphisms are orientation preserving when S is orientable). The elements of MCG(S) are called mapping classes of S. In the case when $S = N_{1,n}$ the mapping class group MCG($N_{1,n}$) is generated by the braid generators σ_i $(1 \leq i \leq n-1)$ and the puncture slides v_i $(1 \leq i \leq n)$ [7]. The braid generator σ_i is a mapping class supported in a disk with two punctures exchanging puncture i and $i+1$ in an anticlockwise manner and leaves the exterior of the disk invariant. Now consider a Möbius band M with a puncture p. The puncture slide v pushes p once along the core curve of M fixing a neighborhood of the boundary of M. The effect of σ_i and the n-th puncture slide v_n on the arcs β_i and β_n are shown in Figure 3. Due to the well-known relation [7] $v_i = \sigma_i v_{i+1} \sigma_i^{-1}$ each mapping class of MCG($N_{1,n}$) can be written as a sequence of braid generators σ_i, the n-th puncture slide v_n, and their inverses. Therefore, each mapping class considered in this paper corresponds to a word where each letter belongs to the set $\{\sigma_1, \sigma_1^{-1}, v_2, v_2^{-1}\}$.

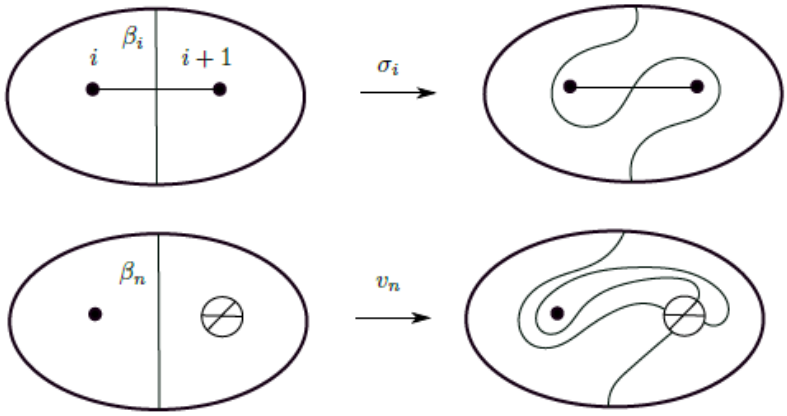

Figure 3. The action of σ_i on β_i and v_n *on* β_n

Definition 2.2. An essential simple closed curve $C \in \mathcal{L}_{1,2}$ is called relaxed if it satisfies one of the following: $\rho(C) = (0; 1; 0)$ or $\rho(C) = (0; -1; 0)$ or C is the core curve of the crosscap as shown in Figure 4.

It is always possible to transform an arbitrary curve in $\mathcal{L}_{1,2}$ into one of the relaxed curves depicted in Figure 4. This process is known as *the relaxation algorithm* for multicurves. Before we give a relaxation algorithm for multicurves in $N_{1,2}$ we present some necessary tools.

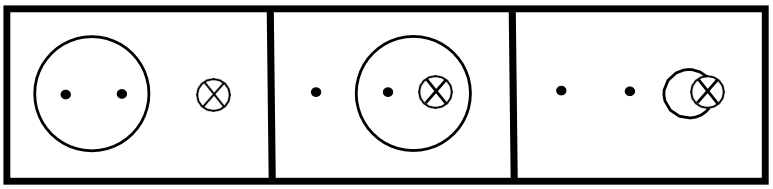

Figure 4. Relaxed curves in $N_{1,2}$

3. Tools for the Algorithm

In this section, we provide some necessary tools to improve the relaxation algorithm in Section 4.

3.1. Dynnikov Coordinates and the action of MCG(D_3)

Removing the crosscap and the arcs $\alpha_{2n-2}, \alpha_{2n-3}$, and β_n from the standard model for the generalized Dynnikov coordinate system depicted in Figure 1, we can construct the Dynnikov coordinate system for the n-punctured disk D_n [3, 5]. For $n \geq 3$, Dynnikov coordinate system [3] provides a bijection ρ: $\mathcal{L}_n \rightarrow \mathrm{Z}^{2n-4}\backslash\{0\}$ from the set of multicurves $\mathcal{L}_n$ in D_n to $\mathrm{Z}^{2n-4}\backslash\{0\}$ given by

$$\rho(\mathcal{L}) \coloneqq (a; b) = (a_1, a_2, \dots a_{n-2}; b_1, b_2, \dots, b_{n-2})$$

where a_i and b_i are as described in equations (1). Since MCG(D_n) is isomorphic to Artin's braid group B_n modulo its center [1] each mapping class of D_3 can be written as a sequence of Artin's braid generators σ_1, σ_2, and their inverses. B_n acts on $\mathcal{L}_n$ piecewise linearly and is described by the *update rules* in terms of the Dynnikov coordinates [3, 4, 5, 6, 8]. Theorem 3.1 gives *updated rules* for B_3.

Theorem 3.1 (Update rules [6]**).** Let $\mathcal{L}$ be a multicurve with $\rho(\mathcal{L}) = (a; b) \in \mathrm{Z}^2\backslash\{0\}$. Let $\rho(\sigma_i(\mathcal{L})) = (a'; b')$ *and* $\rho(\sigma_i^{-1}(\mathcal{L})) = (a'; b')$. *Let* $x^+ = \max(0, x)$. *Then*

- *If* $i = 1$ *then*

$$a' = a + b - max\,(0, a, b)b'$$
$$= b^+ - a$$

- *If* $i = 2$ *then*
- $a' = \max\,(a + b^+, b)$
- $b' = b - a - b^+$
- *If* $i = 1$ *then*

$$a'' = \max\,(0, a + b^+)\text{-}b$$
$$b'' = a + b^+$$

- *If* $i = 2$ *then*
- $a'' = \min\,(a - b^+, -b)$

$$b'' = a + b - b^+$$

Next, we define a move of the algorithm that is only used when $c = 0$.

3.2. Blowdown Move

This move blows down the crosscap to a point labeled p and transforms a multicurve $\mathcal{L}$ in $N_{1,2}$ with generalized Dynnikov coordinates $(a; b; 0) \in \mathbb{Z}^3\backslash\{0\}$ into the same multicurve in D_3 which has hence Dynnikov coordinates $(a; b) \in \mathbb{Z}^2\{0\}$. Suppose that the punctures are labeled 1, 2, and 3 from left to right. Then we say that p is in position 3 or in crosscap position.

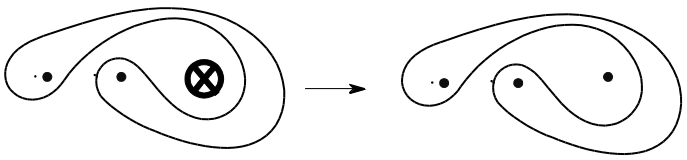

Figure 5. Blowdown move in $N_{1,2}$

4. Relaxation Algorithm

Let $(a; b) \in \mathbb{Z}^2\backslash\{0\}$ (respectively $(a; b; c) \in \mathbb{Z}^3\backslash\{0\}$) be the Dynnikov coordinates (respectively generalized Dynnikov coordinates) of a multicurve $\mathcal{L}$ *in* D_3 (respectively $N_{1,2}$). We write $(a'; b') \in \mathbb{Z}^2\backslash\{0\}$ (respectively $(a'; b'; c') \in \mathbb{Z}^3\backslash\{0\}$ to denote the Dynnikov (respectively generalized Dynnikov coordinates) of $\phi(\mathcal{L})$ where ϕ is a generator of the mapping class group MCG(D_3) (respectively MCG($N_{1,2}$)). Given a multicurve $\mathcal{L} \in \mathcal{L}_{1,2}$ with generalized Dynnikov coordinates $\rho(\mathcal{L}) = (a; b; c) \in \mathbb{Z}^3\backslash\{0\}$ the following algorithm finds a mapping class f such that $f(\mathcal{L})$ is relaxed.

Main Algorithm. **If** $c = 0$ apply Algorithm 1 **otherwise** apply Algorithm 2.

The following algorithm works for the case $c = 0$. The algorithm works with the pair $((a; b), p)$ where p is the position of the labeled puncture p.

Algorithm 1. Given $\mathcal{L} \in \mathcal{L}_{1,2}$ let $\rho(\mathcal{L}) = (a; b; 0) \in \mathbb{Z}^3\backslash\{0\}$.

Step 1: Apply *Blow down* move and replace $(a; b; 0) \in \mathbb{Z}^3\backslash\{0\}$ with $(a; b) \in \mathbb{Z}^2\backslash\{0\}$ and input $((a; b), p)$ to Step 2.

Step 2: If $b \geq 0$ let $(a';b') = \rho(\sigma_1(\mathcal{L}))$ if $a > 0$ and $(a';b')=\rho(\sigma_1^{-1}(\mathcal{L}))$ if $a < 0$. If $a' = 0$ input the pair $((a';b'),p)$ to Step 4: If $a' \neq 0$ and $b' \geq 0$ then input $((a';b'),p)$ to Step 2.
Otherwise, input $((a';b'),p)$ to Step 3.

Step 3: If $b \leq 0$ let $(a';b')=\rho(\sigma_2(\mathcal{L}))$ if $a < 0$ and $(a';b')=\rho(\sigma_2^{-1}(\mathcal{L}))$ if $a > 0$. If $a' = 0$ input $((a';b'),p)$ to Step 4: If $a' \neq 0$ and $b' \leq 0$ then input $\big((a';b'),p\big)$ to Step 3.
Otherwise, input $((a';b'),p)$ to Step 2.

Step 4: Since $a = 0$ then $\mathcal{L}$ is relaxed. **If** $p \neq 3$ let $\rho(\sigma_1\sigma_2\sigma_1)(\mathcal{L}) = (a';b')$ if $p = 1$, and let $\rho(\sigma_2)(\mathcal{L}) = (a';b')$ if $p = 2$. Then input $((a';b'),p)$ to Step 5.

Step 5: Since $a = 0$ and $p = 3$ then $\mathcal{L}$ is a relaxed curve in D_3 with p being in the crosscap position. Blow up p to the crosscap to obtain a relaxed curve in $N_{1,2}$.

The following algorithm works for case $c \neq 0$.

Algorithm 2. Given $\mathcal{L} \in \mathcal{L}_{1,2}$ let $\rho(\mathcal{L}) = (a;b;c) \in \mathbb{Z}^3\backslash\{0\}$ such that $c \neq 0$.

Step 1: If $b \geq 0$ let $(a';b') = \rho(\sigma_1(\mathcal{L}))$ if $a > 0$ and $(a';b')= \rho(\sigma_1^{-1}(\mathcal{L}))$ if $a < 0$.
If $a' = 0$ input $(a';b')$ to Step 3: If $a' \neq 0$ and $b' \geq 0$ then input $(a';b')$ to Step 1.
Otherwise, input $(a';b')$ to Step 2.

Step 2: If $b \leq 0$ let $(a';b') = \rho\big(v_2(\mathcal{L})\big)$ if $a \leq 0$ and $(a';b') = \rho(v_2^{-1}(\mathcal{L}))$ if $a \geq 0$.
If $a' = 0$ and $b' = 0$ input $(a';b')$ to Step 3: If $b' \leq 0$ then input $(a';b')$ to Step 2.
Otherwise, input $(a';b')$ to Step 1.

Step 3: Since $a = 0$, $\mathcal{L}$ is relaxed. Write the generators used in Step 1 and Step 3 in order to express the mapping class f relaxing $\mathcal{L}$.

Remark 4.1. We note that while Algorithm 2 has the advantage of computing the mapping class f relaxing an arbitrary multicurve $\mathcal{L}$, we do not have a tool to describe the action of a puncture slide in terms of generalized Dynnikov coordinates yet.

Conflict of Interest:
The authors declare no conflict of interest.

Publication Ethics:
The authors declare that this document does not require ethics committee approval or any special permission. Our study does not cause any harm to the environment and does not involve the use of animal or human subjects.

Authors' Contributions:

Methodology: F.A, O.Y.

Writing: F.A., A.B., O.Y.

Program Coding: A.B.

All authors read and approved the final manuscript.

References

[1] Artin, E., "Theorie der Zöpfe", *Abh. Math. Sem.*, Univ. Hamburg, 4, 47–72, 1925.

[2] Artin, E., "Theory of braids", *Ann. of Math.*, 48(2), 101–126, 1947.

[3] Dynnikov, I., “On a Yang-Baxter mapping and the Dehornoy ordering”, *Uspekhi Mat. Nauk*, 57(3(345)), 151–152, 2002.

[4] Dehornoy, P., Dynnikov, I., Rolfsen, D., and Wiest, B., Ordering braids, Mathematical Surveys and Monographs, vol. 148, American Mathematical Society, Providence, RI, 2008.

[5] Hall, T., Yurttaş, S. Ö., “On the topological entropy of families of braids”, *Topology Appl.*, 156(8), 1554–1564, 2009.

[6] Hall, T., Yurttaş, S. Ö., “Intersections of multicurves from Dynnikov coordinates”, *Bulletin of the Australian Mathematical Society*, 98(1), 149–158, 2018.

[7] Korkmaz, M., “Mapping class groups of nonorientable surfaces”, *Geom. Dedicata* 89, 109-133, 2002.

[8] Moussafir, J.O., “On computing the entropy of braids”, *Funct. Anal. Other Math.*, 1(1), 37-46, 2006.

[9] Yurttaş, S. Ö., Pamuk, M., “Integral laminations on non-orientable surfaces”, *Turkish Journal of Mathematics*, 42, 69-82, 2018.

[10] Yurttaş, S. Ö., “Curves on non-orientable surfaces and crosscap transpositions”, *Mathematics*, 10(9), 1–33, 2022.

Middle East Journal of Science

https://dergipark.org.tr/mejs **MEJS**

e-ISSN:2618-6136

Research Article

CLOSED BKS-TYPE UNIVERSES AND DIRAC SPIN EFFECT IN THE RAINBOW GRAVITY

Sibel KORUNUR*

Electric-Energy Department, Tunceli Vocational School, Munzur University, Tunceli, Turkey
*Corresponding author; skorunur@munzur.edu.tr

Abstract: *The result related to astrophysical datasets suggest that our universe has recently entered a phase of accelerated expansion. This accelerated expansion is not a situation predicted by the general theory of relativity. Therefore, the emergence of alternative approaches to general relativity has become inevitable. Modifying general relativity and absolute parallelism theory are just two of these theories. In addition, with the discovery of gravitational waves, the need for a view that includes gravitational quantum contributions arose. In this context, rainbow gravity has an approach that also offers quantum contributions to the theory of general relativity and absolute parallelism. In this study, axial vector torsion is calculated for BKS-type universe models using the rainbow gravity formalism. With the calculations made, the vector part and axial vector part components of the torsion tensor are obtained. The spin process, which contributes to the Dirac particle, is also investigated using the rainbow gravitational theory. However, since the obtained axial vector fragment is in time-like form, it is concluded that the spin vector of the Dirac particle is constant. The axial part of the torsion tensor for general BKS-type universe models is calculated and presented in a table for some well-known rainbow functions.*

Keywords: *Absolute parallelism, rainbow gravity, BKS-type universes.*

Received: April 8, 2023 *Accepted: June 7, 2023*

1. Introduction

Torsion is the basis of absolute parallelism theory, which is used as an alternative to the general theory of relativity. While the dynamic basis quantity of the general theory of relativity is the metric tensor, the fundamental quantity of the absolute parallelism theory is tetrads. The unify of gravitational and electromagnetic interaction underlies the absolute parallelism theory by Einstein [1-2]. Weitzenböck connections must be considered when using torsion instead of curvature [3-4]. The torsion tensor describes the textural deformation of space-time, such as the axial-vector part showing how much the axial symmetry deviates from the spherical symmetry [5-6].

Although general relativity and absolute parallelism theories offer some answers to experimental and theoretical astrophysical results, they do not include quantum contributions. Especially with the discovery of gravitational waves, the need for quantum gravity theory has become an indisputable reality. In this context, one of the prominent theories in the literature is the rainbow formalism of gravity [7-8]. According to this formalism, the energy of a test particle creates an effect in the space-time fabric. Thus, a distribution relation with a variable of the form $\epsilon = \frac{E}{E_{Pl}}$ is defined as follows:

$$f_1^2(\epsilon)E^2 - f_2^2(\epsilon)p^2 = m^2. \quad (1)$$

Here $E, m,$ and p are the energy, mass, and momentum of the tested particle, respectively. Also E_{Pl} is represented by the energy of Planck. $f_1(\epsilon)$ and $f_2(\epsilon)$ are known as rainbow functions [7-8]. Recently, many studies have shown the effect of rainbow gravity. The rainbow gravity effect has been studied when the black hole is modified by a particle carrying energy and electric charge [9]. However, many studies have investigated the thermodynamic properties of black holes in the rainbow gravitational framework [10-17]. Various physical properties have been analyzed considering particle equations (Klein-Gordon, Dirac, Photon, etc.) within the framework of rainbow gravity [18-20]. In addition, the thermodynamic phase transition was investigated by applying a quantum correction to the space-time metric in the rainbow of gravity of the Schwarzschild black hole [21]. There are studies examining black string solutions [22] and investigating Hawking radiation from a modified Schwarzschild black hole [23] by considering rainbow gravity.

The Dirac equation can be written in Weitzenböck geometry as below:

$$[h_i{}^{\alpha}\tilde{\gamma}^i(\partial_\mu + \Gamma_\mu) + m]\Psi = 0 \quad (2)$$

where $h_i{}^{\alpha}$ is the tetrad field and $\tilde{\gamma}^i$ are the flat Dirac matrices [24]. The spin connection is represented by Γ_μ and defined as;

$$\Gamma_\mu = \frac{1}{8}[\tilde{\gamma}^i, \tilde{\gamma}^j]h_i{}^{\sigma}h_{j\sigma;\mu} \quad (3)$$

where ";" denotes covariant derivative. The relationship between spin connections (Γ_μ) and vector part (V_μ) and axial vector part (A_μ) is given by [1].

$$\Gamma_\mu = \frac{V_\mu}{2} - \frac{3\mathbb{i}}{4}A_\mu\tilde{\gamma}_5. \quad (4)$$

Here V_μ and A_μ are defined as below respectively,

$$V_\mu = T^{\lambda}{}_{\lambda\mu}, \quad (5)$$

$$A_\mu = \frac{\varepsilon^{\mu\nu\alpha\beta}}{6}T_{\nu\alpha\beta}. \quad (6)$$

$\varepsilon^{\mu\nu\alpha\beta}$ is defined as an antisymmetric Levi-Civita tensor ($\varepsilon^{0123} = 1$) and is related to skew-symmetric tensor ($\delta^{\mu\nu\alpha\beta}$) as follows:

$$\delta^{\mu\nu\alpha\beta} = \frac{\varepsilon^{\mu\nu\alpha\beta}}{\sqrt{-g}}, \quad (7)$$

where g is a determinant of metric tensor ($g_{\mu\nu}$). Variation of the semiclassical spin vector ($\vec{S}$) of Dirac particle with time in terms of space-like axial vector torsion ($\vec{A}$) and spin vector is given by [25]

$$\frac{d\vec{S}}{dt} + \frac{3}{2}\vec{A} \times \vec{S} = \vec{0}. \quad (8)$$

This paper is organized as follows: considering the rainbow formalism, the Dirac spin effect in closed Bianchi Kantowski-Sachs type (BKS-Type) space-time models will be evaluated in the next section. Then calculations will be given in the results and discussion. Finally, the conclusion is devoted to the interpretations of the main results of our research.

2. Materials And Methods

According to the McCallum diagram [26], spatially and homogenous closed universes have been reorganized after the pioneering work of Bianchi [27].

$$ds^2 = -dt^2 + g_{ij}dx^i dx^j \quad (9)$$

The list of BKS-type space-time line elements [28] could be given as

Table 1. The list of Kantowski-Sachs and Bianchi-type space-time line elements (0≤m≤1)

BKS-Types	$g_{ij}dx^i dx^j$
Kantowski-Sachs (KS)	$dx^2 + dy^2 + \sin^2 y\, dz^2$
Bianchi-I (B1)	$dx^2 + dy^2 + dz^2$
Bianchi-II (B2)	$dx^2 + dy^2 + (1+y^2)dz^2 - 2ydxdz$
Bianchi-IV (B4)	$e^{2y}(1+y^2)dx^2 + dy^2 + e^{2y}dz^2 - 2ye^{2y}dxdz$
Bianchi-V (B5)	$e^{2y}dx^2 + dy^2 + e^{2y}dz^2$
Bianchi-VI (B6)	$e^{2(m-1)y}dx^2 + dy^2 + e^{(m+1)}dz^2$
Bianchi-VII (B7)	$e^{2my}dx^2 + dy^2 + e^{2my}dz^2$
Bianchi-VIII (B8)	$(1+2\sinh^2 y)dx^2 + dy^2 + dz^2 + 2\sinh y\, dxdz$
Bianchi-IX (B9)	$dx^2 + dy^2 + dz^2 - 2\sin y\, dxdz$

Now a general form of BKS-type space-time metric could be written in the following format

$$ds^2 = -dt^2 + \mathrm{R}_1^2(y)dx^2 + dy^2 + \mathrm{R}_2^2(y)dz^2 - 2\mathrm{R}_3(y)dxdz. \tag{10}$$

Introducing rainbow functions to general BKS-type metric ($dt \to \frac{dt}{f_1}, dx^i \to \frac{dx^i}{f_2}$) creates the equation (10):

$$ds^2 = -\frac{1}{f_1^2(\epsilon)}dt^2 + \frac{\mathrm{R}_1^2(y)}{f_2^2(\epsilon)}dx^2 + \frac{1}{f_2^2(\epsilon)}dy^2 + \frac{\mathrm{R}_2^2(y)}{f_2^2(\epsilon)}dz^2 - 2\frac{\mathrm{R}_3(y)}{f_1^2(\epsilon)}dxdz. \tag{11}$$

The metric tensor and its reverse are written as follows:

$$g_{\mu\nu} = -\frac{1}{f_1^2(\epsilon)}\delta_\mu^0\delta_\nu^0 + \frac{\mathrm{R}_1^2(y)}{f_2^2(\epsilon)}\delta_\mu^1\delta_\nu^1 + \delta_\mu^2\delta_\nu^2 + \frac{\mathrm{R}_2^2(y)}{f_2^2(\epsilon)}\delta_\mu^3\delta_\nu^3 - \frac{\mathrm{R}_3(y)}{f_1^2(\epsilon)}(\delta_\mu^1\delta_\nu^3 + \delta_\mu^3\delta_\nu^1) \tag{12}$$

$$g^{\mu\nu} = -f_1^2(\epsilon)\delta_0^\mu\delta_0^\nu + \frac{f_2^2(\epsilon)\mathrm{R}_2^2(y)}{\mathrm{R}_1^2(y)\mathrm{R}_2^2(y)-\mathrm{R}_3^2(y)}\delta_1^\mu\delta_1^\nu + f_2^2(\epsilon)\delta_2^\mu\delta_2^\nu + \frac{f_2^2(\epsilon)\mathrm{R}_1^2(y)}{\mathrm{R}_1^2(y)\mathrm{R}_2^2(y)-\mathrm{R}_3^2(y)}\delta_3^\mu\delta_3^\nu$$
$$+\frac{f_2^2(\epsilon)\mathrm{R}_3^2(y)}{\mathrm{R}_1^2(y)\mathrm{R}_2^2(y)-\mathrm{R}_3^2(y)}\left(\delta_1^\mu\delta_3^\nu+\delta_3^\mu\delta_1^\nu\right). \tag{13}$$

Using $g_{\mu\nu} = \eta_{ij}h^i{}_\mu h^j{}_\nu$ relation, the tetrad components of the general BKS-type metric can be obtained in a matrix form as below:

$$h^i{}_\mu = \begin{pmatrix} \frac{1}{f_1} & 0 & 0 & 0 \\ 0 & \frac{R_1}{f_2} & 0 & -\frac{R_3}{f_2} \\ 0 & 0 & \frac{1}{f_2} & 0 \\ 0 & 0 & 0 & \frac{\Im}{f_2 R_1} \end{pmatrix}, \quad h_i{}^\mu = \begin{pmatrix} f_1 & 0 & 0 & 0 \\ 0 & \frac{f_2}{R_1} & 0 & 0 \\ 0 & 0 & f_2 & 0 \\ 0 & \frac{f_2 R_3}{r_1 \Im} & 0 & \frac{f_2 R_1}{\Im} \end{pmatrix}, \tag{14}$$

where we introduced the definition $\Im^2 = R_1^2R_2^2 - R_3^2$.

The axial and vector part depends on the torsion tensor via the Weitzenböck connection ($\Gamma^\lambda{}_{\mu\nu}$) which is defined as follows [29]:

$$\mathrm{T}^\lambda{}_{\mu\nu} = \Gamma^\lambda{}_{\nu\mu} - \Gamma^\lambda{}_{\mu\nu}, \tag{15}$$

and

$$\Gamma^\lambda{}_{\mu\nu} = h_i{}^\lambda \partial_\nu h^i{}_\mu\,. \tag{16}$$

3. 3. Results and Discussions

Considering equation (16), the corresponding non-vanishing components of the Weitzenböck connection are found as follows:

$$\Gamma^1{}_{12} = \frac{\partial_y R_1}{R_1}, \tag{17}$$

$$\Gamma^1{}_{32} = \frac{\Im \partial_y R_3 - R_3 \partial_y \Im}{R_1^2 \Im}, \tag{18}$$

$$\Gamma^3{}_{32} = \frac{R_1 (R_1 \partial_y \Im - \Im \partial_y R_1)}{R_1^2 \Im}. \tag{19}$$

The non-zero components of the antisymmetric torsion tensor become:

$$\mathrm{T}^1{}_{12} = -\mathrm{T}^1{}_{21} = -\frac{\partial_y R_1}{R_1}, \tag{20}$$

$$\mathrm{T}^1{}_{23} = -\mathrm{T}^1{}_{32} = \frac{R_3 \partial_y \Im - \Im \partial_y R_3}{R_1^2 \Im}, \tag{21}$$

$$\mathrm{T}^3{}_{23} = -\mathrm{T}^3{}_{32} = \frac{\partial_y \Im}{\Im} - \frac{\partial_y R_1}{R_1}. \tag{22}$$

Taking account into equations (5-6) and (20-22), the non-vanishing vector part and the axial vector part of torsion are obtained as follows:

$$V_2(y) = -\frac{\partial_y \Im}{\Im} = \frac{R_3 \partial_y R_3 - R_1 R_2 (R_2 \partial_y R_1 + R_1 \partial_y R_2)}{R_1^2 R_2^2 - R_3^2}, \tag{23}$$

$$A_0(y) = \frac{f_1 f_2 (2 R_3 \partial_y R_1 + R_1 \partial_y R_3)}{3 R_1 \Im} = \frac{f_1 f_2 (2 R_3 \partial_y R_1 + R_1 \partial_y R_3)}{3 R_1 \left(R_1^2 R_2^2 - R_3^2\right)^{\frac{1}{2}}}. \tag{24}$$

According to equation (24) axial vector, part of the axial vector torsion behaves time-like form, and space-like form vanishes:

$$\vec{A}(y) = \vec{0}, \tag{25}$$

so the spin vector of the Dirac particle behaves as a constant.

3.1. Special cases

For a particular case discussion of our results, we will use some well-known rainbow functions in the literature. Table 2 shows some rainbow functions frequently encountered in the literature, and the corresponding axial part of the torsion tensor is given for some BKS-type models.

Table 2. Some popular rainbow functions and corresponding axial parts of the torsion tensor.

Cases	Rainbow Functions [30-32] f_1	f_2	BKS-Type	Axial Part
1	$(1-a_3\epsilon)^{-1}$	1	B2	$\frac{e^{2y}(1+2y)}{3\sqrt{1-(e^{4y}-2)y^2+y^4}(a_3\epsilon-1)}$
			B4	$\frac{(1-y^2)}{3(1+y^2)(a_3\epsilon-1)}$
			B6	0
			B8	$\frac{1-2\mathrm{Sech}(2y)}{3-3a_3\epsilon}$
2	1	$1+\frac{\epsilon}{2}$	B2	$-\frac{e^{2y}(1+2y)(2+\epsilon)}{6\sqrt{1-(-2+e^{4y})y^2+y^4}}$
			B4	$\frac{(y^2-1)(2+\epsilon)}{6(1+y^2)}$
			B6	0
			B8	$\frac{1}{6}(2+\epsilon)[1-2\mathrm{Sech}(2y)]$
3	$1+\frac{\epsilon}{2}$	$1+(2\epsilon)^{-1}$	B2	$-\frac{e^{2y}(1+2y)(2+\epsilon)(1+2\epsilon)}{12\sqrt{1-(-2+e^{4y})y^2+y^4}\epsilon}$
			B4	$\frac{(y^2-1)(2+\epsilon)(1+2\epsilon)}{12(1+y^2)\epsilon}$
			B6	0
			B8	$\frac{(1+2\epsilon)[1-2\mathrm{Sech}(2y)]}{6\epsilon}$
4	$(1-a_4\epsilon)^{-1}$	$(1-a_4\epsilon)^{-1}$	B2	$-\frac{e^{2y}(1+2y)}{3\sqrt{1-(-2+e^{4y})y^2+y^4}(-1+\epsilon a_4)^2}$
			B4	$\frac{(y^2-1)}{3(1+y^2)(a_4\epsilon-1)^2}$
			B6	0
			B8	$\frac{1-2\mathrm{Sech}(2y)}{3(a_4\epsilon-1)^2}$

4. Conclusions

Dirac spin effects for various space-time models are a frequently studied topic in the literature [33-36]. In particular, it plays an essential role in developing the theory of absolute parallelism, which is presented as an alternative to general relativity. As can be seen in equation (23), only one component of the vector part of axial vector torsion is non-zero. However, the vector part component has no dependency on the rainbow function. The axial vector part of the axial vector torsion has only a time-like form. However, it does not have a space-like piece. Since the spin vector of the Dirac particle depends on the space-like components of the axial vector torsion, the variation of the spin vector over time remains constant. However, dependence on rainbow functions is observed within the axial vector part. Therefore, the energy of the test particle affects the axial vector torsion. This effect is clearly shown in Table 2:

- For the Bianchi type VI model, the rainbow functions have no effect as the axial vector part is zero.
- According to case 1, the energy of the test particle exerts a reducing effect on the axial vector part for B2, B4, and B8 space-time models.

- For case 2, the energy of the test particle increases the axial vector part for B2, B4, and B8 space-time models.
- Considering the 3rd case, the energy of the test particle increases the axial vector part for B2 and B4 type space-time models and decreases for B8 type space-time model models.
- Finally, considering the 4th case, the energy of the test particle reduces the axial vector part for all the space-time models given in the table.

Ethical Statements

The author declares that this document does not require ethics committee approval or special permission.

Conflict of interest

Author(s) declare no conflict of interest.

Authors Contributions

The author makes all contributions to the manuscript.

References

[1] Hayashi, K. and Shirafuji, T., "New general relativity", *Phys. Rev. D,* 19, 3524, 1979.

[2] Audretsch, J., "Dirac electron in space-times with torsion: Spinor propagation, spin precession, and nongeodesic orbits", *Physical Review D,* 24(6), 1470, 1981.

[3] Hehl, F. W., "How does one measure torsion of space-time?", *Physics Letters A,* 36(3), 225-226, 1971.

[4] Nitsch, J. and Hehl, F. W., "Translational gauge theory of gravity: Post-Newtonian approximation and spin precession", *Physics Letters B,* 90(1-2), 98-102, 1980.

[5] De Andrade, V. C. and Pereira, J. G., "Gravitational Lorentz force and the description of the gravitational interaction", *Physical Review D,* 56(8), 4689 (1997).

[6] Maluf, J. W. and da Rocha-Neto, J. F., "General relativity on a null surface: Hamiltonian formulation in the teleparallel geometry", *General Relativity and Gravitation,* 31(2), 173-185, 1999.

[7] Magueijo, J. and Smolin, L., "Generalized Lorentz invariance with an invariant energy scale", *Physical Review D,* 67, 044017, 2003.

[8] Magueijo, J. and Smolin, L., "Gravity's rainbow", *Classical and. Quantum Gravity,* 21, 1725, 2004.

[9] Gim, Y., and Gwak, B., "Charged black hole in gravity's rainbow: Violation of weak cosmic censorship", *Physics Letters B,* 794, 122, 2019.

[10] Dehghani, M., "AdS4 black holes with nonlinear source in rainbow gravity", *Physics Letters B,* 801, 135191, 2020.

[11] Dehghani, M., "Thermodynamics of charged dilatonic BTZ black holes in rainbow gravity", *Physics Letters B,* 777, 351, 2018.

[12] Dehghani, M., "Thermal fluctuations of AdS black holes in three-dimensional rainbow gravity", *Physics Letters B,* 793, 234, 2019.

[13] Yekta, D. M., Hadikhani, A. and Ökcü, Ö., "Joule-Thomson expansion of charged AdS black holes in Rainbow gravity", *Physics Letters B,* 795, 521, 2019.

[14] Dehghani, M., "Thermodynamic properties of novel dilatonic BTZ black holes under the influence of rainbow gravity", *Physics Letters B,* 799, 135037, 2019.

[15] Gangopadhyay, S. and Dutta, A., "Constraints on rainbow gravity functions from black-hole thermodynamics", *Europhysics Letters*, 115(5), 50005, 2016.

[16] Hamil, B. and Lütfüoğlu, B. C., "Effect of Snyder–de Sitter Model on the black hole thermodynamics in the context of rainbow gravity", *International Journal of Geometric Methods in Modern Physics,* 19(03), 2250047, 2022.

[17] Dehghani, M. and Setare, M. R., "Exponentially charged dilaton black holes in rainbow gravity", *International Journal of Geometric Methods in Modern Physics*, 18(04), 2150063, (2021).

[18] Sogut, K., Salti, M. and Aydogdu, O., "Quantum dynamics of photon in rainbow gravity", *Annals of Physics,* 431, 168556, 2021.

[19] Kangal, E. E., Salti, M., Aydogdu, O., and Sogut, K., "Relativistic quantum dynamics of scalar particles in the rainbow formalism of gravity", Physica Scripta, 96(9), 095301, 2021.

[20] Kangal, E. E., Sogut, K., Salti, M. and Aydogdu, O., "Effective dynamics of spin-1/2 particles in a rainbow universe", *Annals of Physics*, 444, 169018, 2022.

[21] Shahjalal, Md, "Phase transition of quantum-corrected Schwarzschild black hole in rainbow gravity", *Physics Letters B,* 784, 6, 2018.

[22] Dárlla, R., Brito, F. A. and Furtado, J., "Black String solutions in Rainbow Gravity", *arXiv preprint* arXiv:2301.03921. (2023).

[23] Peng, J. J. and Wu, S. Q., "Covariant anomaly and Hawking radiation from the modified black hole in the rainbow gravity theory", General Relativity and Gravitation, 40, 2619, 2008.

[24] Cardall, C. Y. and Fuller, G. M., "Neutrino oscillations in curved space-time: A heuristic treatment", *Physical Review D,* 55(12), 7960 1997.

[25] Nitsch, J. and Hehl, F. W., " Translational gauge theory of gravity: Post-Newtonian approximation and spin precession", *Physics Letters B,* 90(1-2), 98-102, 1980.

[26] McCallum M. A. H., *In General Relativity : An Einstein Centenary Survey,* S.W. Hawking and W. Israel, eds., Cambridge Univ. Press, Cambridge, 1979.

[27] Bianchi, L., "On the three-dimensional spaces which admit a continuous group of motions", *Memorie di Matematica e di Fisica della Società Italiana delle Scienze,* 11, 267-352 (1898).

[28] Fagundes, H. V., "Closed spaces in cosmology", *General Relativity and Gravitation*, 24, 199-217, 1992.

[29] Weitzenböck, R., *Invarianten Theorie,* Noordhoff, Groningen, 1923.

[30] Hendi S.H., et al., "Charged dilatonic black holes in gravity's rainbow", *Eur. Phys. J. C* 76, 1-15, 2016.

[31] Feng, Z. W., and Yang, S. Z., "Thermodynamic phase transition of a black hole in rainbow gravity", *Physics Letters B,* 772, 737-742, 2017.

[32] Leiva, C., Saavedra, J. and Villanueva, J., "Geodesic structure of the Schwarzschild black hole in rainbow gravity", *Modern Physics Letters A,* 24(18), 1443-1451, 2009.

[33] Pereira, J. G., Vargas, T. and Zhang, C. M., "Axial-vector torsion and the teleparallel Kerr space-time", *Classical and Quantum Gravity*, 18(5), 833, 2001.

[34] Korunur, M., Saltı, M., and Aydogdu, O., "An axially symmetric scalar field and teleparallelism", *The European Physical Journal C*, 50(1), 101-107, 2007.

[35] Korunur, M., Salti, M. and Acikgoz, I., "Finding Dirac spin effect in NUT space-time", *Communications in Theoretical Physics*, 53(5), 864, 2010.

[36] Korunur, M., "A non-diagonal singularity-free model in torsion gravity", *Central European Journal of Physics*, 10, 846-849, 2012.

Middle East Journal of Science

https://dergipark.org.tr/mejs **MEJS**

e-ISSN:2618-6136

Research Article

ENHANCED TOTAL PHENOLIC CONTENT EXTRACTION FROM CUCUMIS MELO L. (KULTIK) KERNEL BY DEEP EUTECTIC SOLVENT (DES)

Caglar Mert AYDIN [1] ***Alper GUVEN*** [2]

[1] Food Technology Department, Tunceli Vocational School, Munzur University, TÜRKİYE
[2] Gastronomy and Culinary Arts Department, Faculty of Fine Arts, Design and Architecture, Munzur University, TÜRKİYE
[1] Correspondence author; cmaydin@munzur.edu.tr

Abstract: *The kernel of Cucumis melo L is a by-product produced from the melon production process. The phenolic compounds could be considered as a potential bioactive source for industrial applications. Therefore, the extraction of these compounds as much as possible will decrease valuable waste and could lead to producing value-added products. In the first part of this study, a comparison of the effect of DESs and conventional solvents on total phenolic content (TPC) extraction yield was performed. Some DESs had significantly better extraction yields than conventional solvents. Therefore, optimization of extraction conditions was performed by single factor experiment. Optimized parameters are molar ratio, type of HBA (hydrogen bond acceptor), the addition of water content, extraction time, and extraction temperature. From the results obtained, all these parameters were found to have an impact on TPC extraction yield. Also, it is noteworthy that the extraction yield using some selected parameters was on decreased after a certain extent. The best extraction parameter for Cucumis melo L. was found to be choline chloride as HBA, 1:4 molar ratio, 30% water addition, 50^0 extraction temperature, and 30 min extraction time. This result confirms that kernel of Cucumis melo L. is a valuable ingredient due to its bioactive content, DESs could be a good alternative to conventional solvents and the industrial applications of DESs could be possible.*

Keywords*: Chemistry, Eutectic, Extraction, Green, Kultik.*

Received: January 24, 2023 *Accepted: June 21, 2023*

1. Introduction

Cucumis melo L. (Kultik), one of the melon varieties, has been widely cultivated and consumed in Turkiye. It has a unique kernel, which is shell-less. Even though the fruit of *Cucumis melo* L. is regularly consumed, the kernel was deemed as food waste in Turkiye. Therefore, it has no economic value, leading the kernel of *Cucumis melo* L. to pose serious environmental problems. However, it has many bioactive compounds including valuable phenols [3]. In previous studies, consuming ng kernel of *Cucumis melo* L. was advised due to its bioactive content and was used as an ingredient to produce high-value food products [9,10]. Moreover, utilizing kernel of *Cucumis melo* L. as a source for high-value products is compatible with green extraction technology.

Extraction conditions, including time and temperature, have a major effect to recover phenolic contents in plant materials. Unfortunately, there is no standard method owing to the diverse physicochemical properties of phenolic compounds in plant materials for extraction. Thus, the extraction of each sample must be optimized by specified advantageous conditions for the targeted compound to acquire maximum yield [14]. It is the first time as far as the author knows that the total phenolic content of *Cucumis melo* L. cultivated in Tunceli has been determined.

Conventional solvents were widely used in previous studies to extract phenolic compounds in plant materials [2,25,31]. Differentiation among conventional solvents' properties influences extractable total phenolic content due to secondary metabolites, which show changeable solubility and mass transfer. Methanol, with water as a co-solvent, usually gave the highest TPC in plant materials [14]. However, these solvents have disturbed disadvantages, such as high toxicity and irreversible damage to nature and human life. A ceaseless demand rises to find a green solvent, deemed as an alternative to conventional solvents [5]. Many recent studies showed that deep eutectic solvents (DES) could be a good option for conventional solvents [6,21,30,34]. DESs are mainly formed by mixing hydrogen bond acceptors (HBA) and hydrogen bond donors (HBD). But more components could be added to the formation of DESs. The extraction efficiency of DESs could show differences according to many factors, including types and molar ratios of DES-forming components [21].

This study is targeted to help future studies investigate possible ways solutions for environmental problems caused by food waste and conventional solvents. Therefore, the first objective of this study is to determine the total phenolic content (TPC) of *Cucumis melo* L. by using a conventional solvent (50% Methanol + 50% Water). The second objective is the comparison of TPC extraction efficiency between conventional solvents and DESs to identify whether DES could replace conventional solvents in extraction. The last objective optimizes extraction conditions to achieve maximum TPC yield by DES. Optimized extraction conditions were molar ratio, type of HBA, extraction temperature, extraction time, and co-solvent, namely water, addition.

2. 2. Materials and Methods

2.1. Materials

2.1.1 Sample Preparation Process

Cucumis melo L. kernel used in this study was bought from local producers in Tunceli province, Turkiye during two consecutive years 2021 and 2022 to identify the effect of year variance. After the samples were collected from 5 different producers, they were taken to Munzur University Food Engineering laboratory. The samples were kept at 20^0C in the laboratory.

The sample (at least 250 g) was weighed, then blended by using a kitchen blender (Fisher Scientific, Model 8010ES). All the powder in the blender was mixed. The mixed sample was used for the analyses. The procedure was separately performed for the samples harvested in different years.

2.1.2 Solvent Preparation Process

DESs were prepared according to [16] with some modifications. The components were weighted with various molar ratios in a breaker shortly after they were dried. The breaker was kept in a hot air oven until a homogeneous transparent liquid was formed. The mixture was cooled down to room temperature, then kept at room temperature to store in sealed vessels until their utilization. DES varieties used in this study were displayed in Table 1.

A conventional solvent (50% Methanol + 50% water) was selected for extraction as a comparison to DESs according to the study, which found that phenolic compounds in *Crataegus orientalis* were better extracted with 50% Methanol + 50% water than that with 100% any of conventional solvents [14].

Table 1. Type of DES used in this study.

Type	Combination	Molar Ratio
DES-1	Zinc Chloride: Ethylene Glycerol	1:1
DES-2		1:2
DES-3		1:3
DES-4		1:4
DES-5		1:5
DES-6		1:6
DES-7		1:7
DES-8		1:8
DES-9		1:9
DES-10		1:10
DES-11	Choline Chloride: Ethylene Glycerol	1:4
DES-12	Glucose: Ethylene Glycerol	1:4

2.2. Methods

2.2.1 Total phenolic content

Determination of total phenolic content in the extracts was performed using Singleton's method with some modifications [14]. Briefly, 1 mL of diluted extract was mixed with 5 mL of folin- ciocalteu solution (0.2 N) and vortexed. After the prepared solution was kept dark for 5 minutes, 8 ml of sodium carbonate solution (7.5%) was added to the mix, then the mix was incubated at room temperature for 2 hours. Thereafter, the absorbance values of the samples were measured at 765 nm by UV-Vis spectroscopy. The result was expressed as mg Gallic acid equivalent (GAE) g^{-1} dw of the sample. The standard curve of gallic acid was conducted with various concentrations for each solvent variety used in this study with good linearity (r^2>0.99). For each sample, the Folin-Ciocalteu assay was performed in triplicate.

2.2.2 Determination of optimal extraction conditions

Many factors could affect TPC extraction, but, in this study, three parameters were decided to use by single factor experiment. The effect of the parameters was evaluated according to the statistical analysis result.

2.2.2.1 Evaluation of optimal molar ratio and HBA type

Various molar ratios, including 1:1 to 1:10 HBA-HBD, were utilized. Thereafter, the effect of HBA type on TPC extraction yield was evaluated by using DESs with the best molar ratios (1:4) determined in the earlier part.

2.2.2.2 Evaluation of optimal water content addition to DES

Different water content, ranging from 10% to 50%, was added to determine the effect of water addition to DES. Namely, 10 mL water was added to 100 mL DES to give a 10% water addition.

2.2.2.3 Evaluation of optimal extraction temperature and time

The extraction was performed with DES (70% DES (1:4 molar ratio of ChCI:EtGl) + 30% water), which was determined as the best molar ratio to extract phenolic compounds in the earlier part of this study. Different extraction times (0, 15, 30, 45, and 60 min) were used to compare the effect of extraction time on extraction efficiency at 30^0C, which was chosen by the author according to [6]. Then, the effect

of extraction temperature on TPC extraction was evaluated by using various temperatures (30^0C, 50^0C, 60^0C, and 80^0C) in 30 min, which was determined to be optimal in the earlier part of this study.

Statistical Analysis

All the analyses were performed in triplicate. Each data was subjected to a homogeneity test (Shapiro-Wilk). The results of the test showed that all the data was distributed homogenously; thus, parametric methods were determined to use for all the data found in analyses. Therefore, the data were subjected to analysis of variance (ANOVA) and independent t-test using Statistical Package for Social Science (SPSS) version 29.0 software. Means were separated by using Duncan Multiple Range Test. The level of significance of differences between treatments was determined at $p<0.05$.

3. Results and discussion

Various molar ratios of ZnCI: ethylene glycerol were synthesized to identify the effect of molar ratio on TPC extraction yield. In the first part, 1:1 to 1:10 molar ratios of ZnCI: EtGI were examined, thereafter ZnCI, ChCI, and glucose were used as HBA, and ethylene glycerol was the HBD for understanding the effect of HBA. The increasing HBD molar ratio in the solvent rose the extraction efficiency of phenolic content in the sample to a 1:4 molar ratio, with the highest extraction efficiency of phenolic content being found at a 1:4 molar ratio. A steady decrease in phenolic content extraction was screened from a 1:4 molar ratio to a 1:10 molar ratio of ZnCI: EtGl.

The maximum extraction yield of TPC was determined at a 1:4 molar ratio, 150.24 mg GAE g^{-1} dw in 2021 and 148.21 mg GAE g^{-1} dw in 2022 by ZnCI: Ethylene Glycerol (EtGl). A dramatic and steady decrease was clearly monitored on extracted TPC after the 1:5 molar ratio, with a steady increase being screened from 1:1 to 1:4 molar ratio.

Table 2. Effect of molar ratio parameter on TPC in extracts from *Cucumis melo* L. by Zinc chloride: ethylene glycerol.

Type	Total Phenolic Content (mg GAE g^{-1} dry weight of the sample) 2021	2022	T-test
Conventional Solvent	79.22 ± 9.72e	86.96 ± 5.14e	0.290
DES-1	63.86 ± 3.27d; D	71.71 ± 1.43d; C	0.010
DES-2	91.38 ± 4.68f; E	96.04 ±3.79e; D	0.189
DES-3	112.69 ± 7.82g; F	108.26 ± 5.44f; E	0.466
DES-4	150.33 ± 7.24j; H	148.62 ± 9.05h; G	0.844
DES-5	128.16 ± 5.54h; G	119.93 ± 5.19g; F	0.064
DES-6	27.40 ± 2.17c; C	26.14 ± 1.03b, c; B	0.388
DES-7	23.16 ± 2.62b, c; B,C	20.82 ± 1.78a, b; A,B	0.299
DES-8	15.73 ± 1.52 a, b; A, B	15.22 ± 0.69a, b; A	0.626
DES-9	12.17 ± 1.91a, b; A	12.44 ± 2.48a; A	0.885
DES-10	10.62 ± 0.60a; A	11.92 ± 0.79a; A	0.086

Note: Different letters in the same column show a significant difference ($p< 0.05$).
Lower case: it was used for the solvents including conversational solvents and different molar ratios of ZnCI: EtGI.
Upper case: it was used for ANOVA analysis of DESs having the same HBA with different molar ratios

It is noticeable that some DESs significantly better extracted TPC than the conventional solvent. A 1:4 molar ratio was found the most favorable for the best extraction yield. Significant differences among different molar ratios of ZnCI: EtGl were found, with year variance causing no significant influence on TPC extraction yield, except for the 1:1 molar ratio. The exception might be related to the difference in the solvent's polarity, which could affect the molar ratio of DES [1,15]. Ozturk et. al. [28]

stated that the extraction yield of TPC from orange peel waste changed with regard to the polarity, which showed a difference according to the molar ratio of DESs. This result is in according with the study of Li et. al. [23], which observed that a 1:4 molar ratio is the best for TPC extraction yield for amino acid-based DESs. Moreover, some DESs of ZnCI: EtGl with different molar ratios showed significantly better extraction yield than conventional solvent, which was expressed to be the best conventional solvent for extraction from plant materials [14]. This result means that DESs could have a chance to take the place of conventional solvents in TPC extraction from plant materials. It is a need to state that, as far as the author's experience, using 1:1 and 1:2 molar ratios of HBA: HBD was extremely difficult for TPC extraction due to high viscosity. Even though a constant acceleration on TPC was observed from 1:1 to 1:4 molar ratio, a catastrophic decrease screened on TPC extraction yield by DES after 1:5 molar ratio. This result could be related to low viscosity, which was reported not to be appropriate to extract target compounds [24].

Results of previous studies showed differentiation for the best molar ratio of DES in TPC extraction. Some studies, which are in according with this study, stated that 1:4 molar ratio of HBD:HBA gave the highest extraction efficiency of phenolic content in plant materials [21,30]. However, Luo et. al. [25] demonstrated that the highest phenolic content was found in green tea (*camellia sinesis*) extracted by the combination of ultrasonic-assisted extraction and a 1:2 molar ratio of choline chloride: glycerol. Chen et. al. [12] reported that extraction yield for the selected compound from Radix *salviae miltiorrhizae* steadily decreased as the molar ratio of ChCI used as HBA was on the decrease, and that 1:3 molar ratio of ChCI: glycerol had better extraction efficiency than 1:4 molar ratio. The differences in the results of the studies could be due to many factors, including the part of plant materials, the plant growing conditions, and even the extraction process [31,38]. In addition, the differences in DES extraction yield may happen due to structural differences, which could be easily modified by the choice of DES-forming components shaping hydrogen bond constitution [37].

To evaluate the effect of HBA type on TPC extraction yield, choline chloride (ChCI) and glucose were used in comparison to ZnCI. A 1:4 molar ratio was determined to use for comparison of HBA type due to the result in the early part of this study. It was found that HBA type in DES could significantly affect TPC extraction yield in plant material, with ChCI: EtGI significantly having higher extraction yield when glucose: EtGI significantly having the lowest extraction efficiency, $p<0.01$. ChCI as HBA was also observed as the best for TPC extraction by many previous studies [2,8,12,36]. Thus, it is necessary to express that even though many studies just focused on the type of HBD for better extraction yield and reported that type of HBD mainly affects extraction yield [7,22,29,33], this study found that the type of HBA also has a precise effect on extraction yield.

Table 3. Effect of HBA (Hydrogen bond acceptor) parameter on TPC in extract from *Cucumis melo* L.

Type	Total Phenolic Content (mg GAE g^{-1} dry weight of the sample)		T-test
	2021	2022	
DES - 4	150.33 ± 7.24b	148.62 ± 9.05b	0.844
DES-11	163.34 ± 12.73c	162.76 ± 6.00c	0.961
DES-12	27.40 ± 6.37a	32.27 ± 4.50a	0.341

The extraction yield of phenolic components available in foods could be enhanced depending on extraction conditions and suitable co-solvent usage [32]. Many studies reported that conventional solvents with a co-solvent were more effective in TPC extraction [4,35]. The addition of co-solvent to DES was mentioned to have the potential to increase extraction efficiency in plant materials due to better solvent penetration into the sample [40]. Thus, in order to determine the effect of adding a co-solvent,

namely water, to DES on TPC extraction, a 1:4 molar ratio of ChCI: EtGl was decided to use due to that it gave the highest phenolic content from *Cucumis melo* L kernel in the earlier part of this study. TPC extraction was performed with DES containing different percentages of water ranging from 10% to 50%. The yields of TPC extracted by any combination of DES and water from *Cucumis melo* L kernel were significantly higher than DES without any water addition. It could be due to that adding water to DES could reduce viscosity, and lower viscosity led to higher mass transfer [19]. The same result was also found in previous studies [27,34,37,39]. Moreover, there wasn't any significant difference among DESs including various water content, with 70% DES + 30% water having the highest extraction yield than any combination of DES and water. Even though it wasn't significant (p>0.05), higher than 30% water addition to DES led to lower extraction yield in this study. The same result was also observed by previous studies [12,20,27,39,42]. Chen et. al. [12] enhanced the extraction efficiency of the selected compounds by adding water to ChCI-1,2-Propanediol up to a certain extent. Wu et. al. [36] stated that adding higher than 40% water to DES led to lower TPC extraction yield in *Polygonum aviculare* leaves. New et. al. [27] emphasized that maximum extraction efficiency of lignin was found for DES (ChCI-Urea) including 20% water content. The increase in extraction efficiency as water content rises to a certain extent might be owing to better solvent penetration and diffusion of the solute targeted in the sample [42]. The lower extraction yield after a certain extent could be related to the interaction between co-solvent and CO_2 [13] or destroying effect of co-solvent concentration on the hydrogen bonds between DES-forming components [17]. In addition, Chen et. al. [12] indicated that as the water content in DES was on the increase, better extraction yield was observed for hydrophilic compounds up to a certain extent (60%-80% water content, depending on the targeted component) when water extraction yield was monitored for hydrophobic compounds. The differences among the studies reveal that extraction of TPC in the sample needs an individual approach.

Table 4. Effects of extraction parameters on TPC in extracts from *Cucumis melo* L.

Factors	**Total Phenolic Content (mg GAE g^{-1} dry weight of the sample)**	
Water Content*	2021	2022
10%	245.46 ± 8.22a	221.67 ± 41.11a
20%	253.86 ± 14.67a	236.47 ± 21.60a, b
30%	282.48 ± 20.40b	277.59 ± 15.07b
40%	265.81 ± 4.44a, b	251.69 ± 20.87a, b
50%	257.59 ± 13.71a, b	228.38 ± 24.29a, b
Extraction Time**		
0 min	282.48 ± 20.40a	277.59 ± 15.07a
15 min	311.22 ± 14.13a	286.49 ± 12.74a
30 min	398.36 ± 32.82b	379.52 ± 24.81b
45 min	399.54 ± 21.19b	381.87 ± 45.10b
60 min	417.20 ± 14.13b	392.47 ± 40.74b
Extraction Temperature***		
30^0C	398.36 ± 32.82a	379.52 ± 24.81a
50^0C	814.96 ± 12.50c	719.67 ± 12.10c
60^0C	567.86 ± 12.12b	504.46 ± 4.98b
80^0C	524.74 ± 31.81b	407.72 ± 15.22a

Note: Different letters in the same column show a significant difference (p < 0.05). *Extraction conditions: L/S ratio: 100:1 mL/mg; extraction temperature: 30°C; extraction time: 0 min; **Extraction conditions: L/S ratio: 100:1 mL/mg; Water content: 30%; temperature: 30°C; ***Extraction conditions: L/S ratio: 100:1 mL/mg; Water content: 30%; extraction time: 30 min.

Extraction time was evaluated using various times ranging from 0 minutes to 60 minutes. Extraction time was found to affect TPC extraction yield. Just after mixing DES (70% DES + 30% water) with the sample, TPC was found to be 282.48 mg g^{-1} dw for kernels harvested in 2021: and 277.59 mg g^{-1} dw for kernels harvested in 2022. Extracted TPC was on the increase as extraction time was on the increase. Extraction time is also an important parameter in TPC extraction from plant materials. Generally, shorter extraction time with the same extraction yield is demanded enhanced process applications [23]. A significant change in extraction yield according to extraction time was observed, with no significant difference being found after 30 min. This result is in according with the result of previous studies [11,26,37,42]. Even though Wu et. al. [36] didn't find any significant difference among extraction times of 30, 40, and 50 minutes, Mansinhos et. al. [26] stated that even if there was not a significant difference between 15 min and 30 min of extraction times, 60 min having significantly better TPC extraction yield. Zhou et. al. [42] also found the same result, which showed no significant difference between 15 min and 30 min of extraction time for some of the phenolic compounds from *Morus alba* L., with [26]. The difference among the studies could rise due to the extraction process, which was differently done.

Temperature is one of the key factors leading to changes in extraction yield. The effect of temperature on TPC extraction by the DES (70% DES (ChCI- ethylene glycerol, 1:4 molar ratio) + 30% Water) was investigated. To evaluate the effect of extraction temperate, temperatures ranging from 30^0 to 80^0 were performed. Extraction time was chosen as 30 min according to the early part of this study, which found that there wasn't any significant difference in TPC extraction yield after 30 min (Table 4). The highest TPC was found at 50^0 extraction temperatures. The extraction yield of TPC by DES regularly decreased as the extraction temperature rose after 50^0. Extraction temperature was determined to have an impact on extraction yield. In previous studies, it was stated that a rise in the extraction temperature within a specific range usually led to lower viscosity of DES, which enhances better mass transfer, and eventually higher analyte solubility [18]. In this study, a significant difference was determined among extraction temperatures for extraction yield of TPC, with the highest TPC being found at 50^0 extraction temperatures. It is eye-catching that the extraction yield of TPC by DES regularly decreased as the temperature rose after 50^0. The same result, the decrease in the yield after 50^0, was also demonstrated by previous studies [20,23,36,37]. However, Bildik [6] and Zhou et. al. [42] monitored the same decrease in TPC extraction of Rheum Ribes leaves by ChCI-based DESs just after 40^0. The reason why the TPC value was on the decrease as extraction temperature was on the increase after a certain extent could be due to lower mass transfer [16]. In addition, extraction conditions led to the difference in the study of [6] and [42] which used ultrasound-assisted extraction. Zhou et. al. [42], which used extraction temperatures ranging from 30^0 to 60^0, found the lowest extraction yields of phenols at 30^0. This result is in accordance with the result found in this study. High or low extraction temperatures may negatively influence the stabilization capacity of the extraction assay, which changed due to the low or high viscosity of DES, and this may lead to limited mass transfer [16].

4. Conclusions

This study found that *Cucumis melo* L kernel has high total phenolic content, which makes it an important substance for the extraction process. TPC of the sample had 79.22 mg GAE g^{-1} dry weight in 2021, and 86.96 mg GAE g^{-1} dw in 2022 by conventional solvent (50% methanol + 50% water).

Twelve DES varieties were used in this study to compare TPC extraction yield to conventional solvent. It was found that some DESs could better extract TPC in the sample than conventional solvents. This result represents an enormous opportunity for the utilization of DESs in industrial applications.

Optimization of TPC extraction conditions using DES was also investigated by single-factor experiments. The molar ratio of DES was found to have a significant effect on TPC extraction yield.

The highest TPC was found at the 1:4 molar ratio of the DES type investigated. Further, the DES-forming component as HBA was observed to change extraction yield, with ChCI having statistically the best extraction yield. Moreover, it was important to note that a higher than 1:5 molar ratio caused a dramatic reduction in the extraction yield of TPC.

Adding a co-solvent, namely water, has been reported to affect extraction yield by DES. All the combinations of DES and water showed better extraction efficiency than the DES without any addition of co-solvent. The highest total phenolic content extraction was determined for 70% DES + 30% water. TPC extraction yield was on the increase as water content was on the increase by up to 30% water addition. It is important to state that even though it was not significant, higher water content than 30% could lead to a decrease in TPC extraction yield.

Extraction temperature and time were also game-changing factors. The highest extraction yield was obtained at 50^0 with 30 min extraction time. It was important that TPC extraction yield was on the decrease as extraction temperature was on the increase after 50^0. Additionally, 30 min of extraction time had statistically better extraction yield than 0 and 15 min of extraction time. Even though extraction yield was on the increase as extraction time was on the increase, no statistically significant difference was found between 30 min extraction time and any of more than 30 min extraction time.

Therefore, the method proposed in this study provides a possible pathway to green extraction of bioactive compounds from plant materials, particularly those being accepted as food waste, but having huge potential for industrial applications. Further studies are needed to identify any possible correlation of the parameters used in this study with some antioxidant assays.

Conflict of Interest

The authors declare no conflict of interest.

Ethical statements

The authors declare that this document does not require ethics committee approval or any special permission. Our study does not cause any harm to the environment and does not involve the use of animal or human subjects.

Authors' Contributions

AYDIN C. M.: Conceptualization, Data curation, Formal analysis, Investigation, Methodology, Software, Writing – original draft, Visualization, Validation.

GUVEN A.: Validation, Project administration, Software, Review and editing.

References

[1] Abbott, A.P., Harris, R.C., Ryder, K.S., D'Agostino, C., Gladden, F., Mantle, M.D., "Green chemistry glycerol eutectics as sustainable solvent systems*", Green Chem*., 13 (1), 82−90, 2011. doi: 10.1039/C0GC00395F

[2] Almeida, P.P.V., Shiwaku, I.A., Maximo, G.J., Batista, E.A.C., "Choline chloride-based deep eutectic solvents as potential solvent for extraction of phenolic compounds from olive leaves: Extraction optimization and solvent characterization", *Food Chemistry*, Vol. 352, 129346, 2021. doi: 10.1016/j.foodchem.2021.129346.

[3] Aydin, C.M., Güven, A., "Tunceli ilinde yetiştirilen kultik çekirdeğinin bazı fizikokimyasal özelliklerinin belirlenmesi", *International Malatya gastronomy culture and tourism conference,* Malatya, Turkiye, 1(16-18), 202- 210, 2022.

[4] Barbosa, A.M., et. al., "Separation of antibacterial biocompounds from *Hancornia speciosa* leaves by a sequential process of pressurized liquid extraction", *Sep Purif Technol.,* 222, 390–395, 2019. doi: 10.1016/j.seppur.2019.04.022.

[5] Baranse, O., Parkinson, C., Gonzalez, M.M., "Extraction of polyphenolic antioxidants from orange peel waste using deep eutectic solvents", *Separation and Purification Tech.*, 206, 1-13, 2018. doi: 10.1016/j.seppur.2018.05.052.

[6] Bildik, F., "Application of choline chloride as natural deep eutectic solvents for the green extraction of phenolic compounds from rheum ribes leaves", *European Journal of Technique*, 11 (2), 140- 143, 2021. doi: 10.36222/ejt.960412.

[7] Busic, V., Molnar, M., Tomicic, V., Bozanovic, D., Jerkovic, I., Gaso-Sokac, D., "Choline chloride-based deep eutectic solvents as green effective medium for quaternization reactions", *Molecules*, Vol. 27(21), 7429, 2022. doi: 10.3390/molecules27217429.

[8] Cao, J., Chen, L., Li, M., Cao, F., Zhao, L., Su, E., "Efficient extraction of proanthocyanidin from Ginkgo biloba leaves employing rationally designed deep eutectic solvent-water mixture and evaluation of the antioxidant activity", *Journal of Pharmaceutical and Biomedical Analysis*, 158, 317–326, 2018. doi: 10.1016/j.jpba.2018.06.007.

[9] Celik, I., Kuzumoglu, Y., "Farklı tane unları ve cekirdek tozları kullanılarak glutensiz lokma tatlısı üretimi ve kalite özellikleri", *Akademik Gıda*, 18 (2), 156-163, 2020. doi: 10.24323/akademik-gida.758828.

[10] Celik, I., Pozan, K., "Kavun çekirdeği tozunun eriştenin bazı özelliklerine etkisi", *The Journal of Food*, 45 (5), 907- 916, 2020. doi: 10.15237/gida.gd20038.

[11] Charpe, T.W., Rathod, V.K., "Kinetics of ultrasound assisted extraction of wedelolactone from *Eclipta alba*", *Braz. J. Chem. Eng.*, 33, 1003–1010, 2016. doi: 10.1590/0104-6632.20160334s20140234.

[12] Chen, J., Liu, M., Wang, Q., Du, H., Zhang, L., "Deep eutectic solvent-based microwave-assisted method for extraction of hydrophilic and hydrophobic components from radix salviae miltiorrhizae", *Molecules*, Vol. 21, 1383, 2016. doi: 10.3390/molecules21101383.

[13] Chupin, L., Maunu, S.L., Reynaud, S., Pizzi, A., Charrier, B., Bouhtoury, F.C., "Microwave assisted extraction of maritime pine (*Pinus pinaster*) bark: Impact of particle size and characterization", *Ind. Crop. Prod.*, 65, 142- 149, 2015. doi: 10.1016/j.indcrop.2014.11.052.

[14] Coklar, H., Akbulut, M., "Alıç (Crataegus orientalis) meyvesinin antioksidan aktivitesi ve fenolik bileşiklerinin ekstraksiyonu üzerine farklı çözgenlerin etkisi", *Derim*, 33 (2), 237-248, 2016. doi: 10.16882/derim.2016.267908.

[15] Craveiro, R., et. al., "Properties and thermal behavior of natural deep eutectic solvents", *J.Mol. Liq*, 215, 534−540, 2016. doi: 10.1016/j.molliq.2016.01.038.

[16] Dai, R., Verpoorte, Y., Choi, H., "Natural deep eutectic solvents providing enhanced stability of natural colorants from safflower (*Carthamus tinctorius*)", *Food Chem.*, 159, 116–121, 2014. doi: 10.1016/j.foodchem.2014.02.155.

[17] Dai, Y., Witkamp, G.J., Verpoorte, R., Choi, Y.H., "Tailoring properties of natural deep eutectic solvents with water to facilitate their applications", *Food Chemistry*, 187, 14-19, 2015. doi: 10.1016/j.foodchem.2015.03.123.

[18] Dai, J., Mumper, R.J., "Plant phenolics: extraction, analysis and their antioxidant and anticancer Properties", *Molecules*, 15 (10), 7313- 7352, 2010. doi: 10.3390/molecules15107313.

[19] Gao, M.Z., et. al., "A green and integrated strategy for enhanced phenolic compounds extraction from mulberry (*Morus alba* L.) leaves by deep eutectic solvent", *Microchemical Journal*, 154, 104598, 2020. doi: 10.1016/j.microc.2020.104598.

[20] Hsieh, Y.H., et. al., "Ultrasonication-assisted synthesis of alcohol-based deep eutectic solvents for extraction of active compounds from ginger", *Ultrasonics Sonochemistry*, 63, 104915, 2019. doi: 10.1016/j.ultsonch.2019.104915.

[21] Jablonsky, M., Majova, V., Strizincova, P., Sima, J., Jablonsky, J., "Investigation of total phenolic content and antioxidant activities of spruce bark extracts isolated by deep eutectic solvents", *Crystals*, 10(5), 402, 2020. doi: 10.3390/cryst10050402.

[22] Krisanti, E.A., Saputra, K., Arif, M.M., Mulia, K., "Formulation and characterization of betaine-based deep eutectic solvent for extraction phenolic compound from spent coffee grounds", *AIP Conference proceedings*, 2175 (1), 020040, 2019. doi: 10.1063/1.5134604.

[23] Li, M., Liu, Y., Hu, F., Ren, H., Duan, E., "Amino acid-based natural deep eutectic solvents for extraction of phenolic compounds from aqueous environments", *Processes*, 9(10), 1716, 2021. doi: 10.3390/pr9101716.

[24] Liu, Y., Li, J., Fu, R., Zhang, L., Wang, D., Wang, S., "Enhanced extraction of natural pigments from *Curcuma longa* L. using natural deep eutectic solvents", *Industrial Crops and Products*, 140, 111620, 2019. doi: 10.1016/j.indcrop.2019.111620.

[25] Luo, Q., et. al., "Green extraction of antioxidant polyphenols from green tea (*Camellia sinesis*)", *Antioxidant*, 9(9), 785, 2020. doi: 10.3390%2Fantiox9090785.

[26] Mansinhos, I., Goncalves, S., Rodriguez-Solana, R., Ordonez-Diaz, JL., Moreno-Rojas, J.M.,Romano, A, "Ultrasonic-assisted extraction and natural deep eutectic solvents combination: A green strategy to improve the recovery of phenolic compounds from *Lavandula pedunculata subsp. Iusitanica* (Chaytor) Franco", *Antioxidants*, 10(4), 582, 2021. doi: 10.3390/antiox10040582.

[27] New, E.K., et. al., "Potential use of pure and diluted choline chloride-based deep eutectic solvent in delignification of oil palm fronds", *Process Safety and Environmental Protection*, 123, 190–198, 2019. doi: 10.1016/j.psep.2018.11.015.

[28] Ozturk, B., Parkinson, C., Gonzalez-Miquel, M., "Extraction of polyphenolic antioxidants from orange peel waste using deep eutectic solvents", *Separation and Purification Technology, 206*, 1–13, 2018. doi: 10.1016/j.seppur.2018.05.052.

[29] Picchio, M.L., et. al., "Natural deep eutectic solvents based on choline chloride and phenolic compounds as efficient bioadhesives and corrosion protectors", *ACS Sustainable Chem. Eng*, 10 (25), 8135- 8142, 2022. doi: 10.1021/acssuschemeng.2c01976.

[30] Rida'I, M.T.A.A., Tulaphol, S., Thanasupsin, S.P., "Choline chloride based deep eutectic solvent, a green solvent for extraction of phenolic compound from coffee silverskin", *PACCON Pure and Applied Chemistry International Conference,* Nonthanburi, Thailand, Vol 1, 2020.

[31] Spinelli, S. et. al., "Bioactive compounds from Norway spruce bark: comparison among sustainable extraction techniques for potential food application", *Foods*, 8(11), 524, 2019. doi: 10.3390/foods8110524.

[32] Strizincova, P. et. al., "Spruce Bark-A source of polyphenolic compounds: Optimizing the operating conditions of supercritical carbon dioxide extraction", *Molecules*, 24(22), 4049, 2019. doi: 10.3390/molecules24224049.

[33] Torres, P., Balcells, M., Cequier, E., Canela-Garayoa, R., "Effect of four novel bio-based DES (deep eutectic solvents) on hardwood fractionation", *Molecules*, 25(9), 2157, 2020. doi: 10.3390/molecules25092157.

[34] Xu, M., Ran, L., Chen, N., Fan, X., Ren, D., Yi, L., "Polarity- dependent extraction of flavonoids from citrus peel waste using a tailor-made deep eutectic solvent", *Food Chemistry*, 297, 124970, 2019. doi: 10.1016/j.foodchem.2019.124970.

[35] Vitor, D., Tarone, A.G., Betim, C., Fernandez, G., Martínez, J., "Pressurized liquid extraction of bioactive compounds from grape marc", *J Food Eng*, 240, 105–113, 2019. doi: 10.1016/j.jfoodeng.2018.07.019.

[36] Wu, L., Chen, Z., Li, S.,Wang, L., Zhang, J., "Eco-friendly and high- efficient extraction of natural antioxidants from *Polygonum aviculare* leaves using tailor-made deep eutectic solvents as extractants", *Separation and Purification Technology*, 262, 118339, 2021. doi: 10.1016/j.seppur.2021.118339.

[37] Yazici, S.O., Ozmen, I., "Ultrasound assisted extraction of phenolic compounds from Capparis ovata var canescens fruit using deep eurecti solvents", *J. of Food Processing and Preservation*, 46 (11), 1-14, 2021. doi: 10.1111/jfpp.16286.

[38] Yılmaz, M.S., Kutlu, N., Erdem, GM., Sakiyan, O., Isci, A., "Fenolik bileşiklerin alıç meyvesinden (*Crategus monogyna*) mikrodalga ve ultrases destekli yöntemler ile ekstraksiyonu", *Gıda*, 46 (4), 1002- 1015, 2021. doi: 10.15237/gida.GD21018.

[39] Zhang, L., Wang, M., "Optimization of deep eutectic solvent-based ultrasound-assisted extraction of polysaccharides from Dioscorea opposita Thunb", *International Journal of Biological Macromolecules*, 95, 675–681, 2017. doi: 10.1016/j.ijbiomac.2016.11.096.

[40] Zhao, Z., Moghadasian, M., "Chemistry, natural sources, dietary intake and pharmacokinetic properties of ferulic acid: A review", *Food Chemistry*, 109, 691-702, 2008. doi: 10.1016/j.foodchem.2008.02.039.

[41] Zeng, J., Dou, Y., Yan, N., Li, N., Zhang, H., Tan, J., "Optimizing ultrasound-assisted deep eutectic solvent extraction of bioactive compounds from Chinese wild rice", *Molecules*, 24 (15), 2718, 2019. doi: 10.3390/molecules24152718.

[42] Zhou, P. et. al., "Enhanced phenolic compounds extraction from *Morus alba* L. leaves by deep eutectic solvents combined with ultrasonic-assisted extraction", *Industrial Crops and Products*, 120, 147–154, 2018. doi: 10.1016/j.indcrop.2018.04.071.

Middle East Journal of Science

https://dergipark.org.tr/mejs **MEJS**

e-ISSN:2618-6136

Research Article

A PROPOSED SMART IRRIGATION MANAGEMENT SYSTEM BASED ON THE IOT AND CLOUD COMPUTING TECHNOLOGIES

Waseem HAMDOON*[1] Ahmet ZENGIN[1]

[1]Sakarya University, Faculty of Computer and Information Engineering, Sakarya, Türkiye
*Corresponding author: waseem.algburi@ogr.sakarya.edu.tr

Abstract: *Most fresh water is used in agriculture. There has been a constant interest in presenting systems and solutions that rationalize water resources in agriculture without reducing productivity. In contrast, the solutions must improve production while utilizing less water. On the other hand, The Internet of Things is a prominent recent technology that provides various solutions in many disciplines, including agriculture and irrigation. This paper proposes an Internet-of-Things-based architecture for smart irrigation by developing a prototype with a controller unit, water pumps, and sensors. These systems monitor the soil's irrigation needs and determine the right amount based on sensor data. As these values are delivered through cloud computing to a user's mobile app, irrigation may be monitored and controlled from multiple angles. This comprises manual irrigation mode and automatic irrigation mode and determines the right amount of irrigation based on sensor relationships.*

Keywords*: Internet of Things; Cloud Computing; Smart Irrigation; Actuators; Sensors.*

Received: July 22, 2022 *Accepted: June 26, 2023*

1. Introduction

Agriculture is the main source of food and, at the same time, the largest consumer of fresh water, consuming up to 70% of all water resources [1]. Where this high percentage of water consumption explains the reason for the increasing interest by researchers in the possibility of reducing the use of irrigation water [2]. Several concepts emerged around this, including "sustainable irrigation," one of the main concerns for preserving water resources through wise policies in rationalizing water consumption [3]. Contrarily, inefficient irrigation practices have several detrimental effects, the biggest among them water waste and a decrease in the quality of the crops that are produced, particularly when irrigation is irregular [8] and does not take into account the demands of each plant or crop separately. Mostly, there is more than one type of plant in the fields and each type requires a different amount of water [9]. In many cases, farmers pump more water than is required (excessive irrigation), which leads to lower production as well as the waste of water and energy [10].

On the other hand, the use of Internet of Things technology has grown significantly in recent years, and as a result, there have been more and more devices connected to the Internet as a result of the need to collect data from these devices for various Internet of Things applications [4]. It is estimated that the number of connected devices will reach 25.1 billion by 2025 [5]. In the field of irrigation, IoT offers various applications to monitor crop growth and support irrigation decisions [6], making it a logical choice for smart water management applications. Currently, despite the spread of IoT, there are still some challenges that prevent the widespread use of IoT for precision irrigation, such as the need to

develop software for IoT-based smart applications, and the need to automate irrigation processes using dedicated platforms which is not yet fully automated [7], and so on.

In this study, a proposal for a smart irrigation system based on the Internet of Things was presented, through which the appropriate amount of irrigation can be controlled, as well as the appropriate irrigation time, considering the weather conditions of the crop and soil.

Although there are many studies or proposed systems in this field, however, there are problems in representing these proposed systems, most notably: (1) Adopting fixed boundary values at which the irrigation decision is taken, which cannot be changed easily or at any time according to the supervisor of the irrigation process. (2) The amount of irrigation is fixed for all crops/plants without taking into account the existence of a difference in the amount of water required for each, (3) The amount of irrigation is fixed - non-dynamic - for a single crop/plant without taking into account the difference in other factors affecting the soil, such as (soil temperature, air humidity, air temperature) and their impact on determining the appropriate amount based on those variable values. Accordingly, this study attempts to overcome these problems by proposing a new irrigation architecture based on the Internet of Things, as well as some other additional features that increase the efficiency of irrigation management.

2. Material and Methods

The techniques used to represent the proposed system are briefly discussed in this section.

2.1. Hardware

Most IoT-based systems are made up of three fundamental parts: a controller, a sensor, and an actuator, in addition to a middle layer to enable the control unit to connect to the Internet to send the data gathered as well as instructions that are required.

2.1.1 Controller

It is usually used to automatically control devices and equipment [11]. The controller in IoT applications is like the brain, processing inputs from sensors or other sources and producing outputs from one of the actuators. In this study, the “Raspberry Pi 3 Model B” is employed as a controller. The Raspberry Pi Foundation, in collaboration with Broadcom, has produced a line of miniature single-board computers (SBCs). Initially, the Raspberry Pi project aimed to promote basic computer science education in schools and impoverished countries. Its low cost, versatility, and open design make it popular in many fields, including weather monitoring [12][13].

2.1.2 Sensors

Sensors are essential in automating any application since they collect data and process it [11].

- **Soil Moisture Sensor**

A “Capacitive Soil Moisture v2.0” sensor is used to measure the soil's moisture level. This capacitive sensor has excellent responsiveness to local soil moisture changes and provides an effective correlation between gravimetric water content and output voltage [14][15].

- **Soil temperature sensor**

To measure the soil temperature, a sensor of the type DS18B20 is used. It is a digital temperature sensor, used in many applications and difficult environments. The startup resolution is 12 bits, where there is a resolution of 9, 10, 11, or 12 bits, which means the temperature sensor can accurately measure temperatures of 0.25°C, 0.125 °C, and even 0.0625°C [16][17].

- **Air temperature and humidity sensor**

A sensor of type DHT11 is used to monitor and measure the temperature and humidity of the surrounding environment of a field or crop [17]. The DHT11 is a popular temperature and humidity

sensor that features a dedicated (NTC) for measuring temperature as well as an 8-bit microprocessor for outputting the values of temperature and humidity as serial data [18][19].

2.1.3 Actuators

On the Internet of Things, actuators use data received by sensors and processed by software to control or take action in the system [20].

- **Water pump**

A water pump is used for the purpose of irrigating the crop or field when the threshold limit is reached.

2.2. Software

It is typical for Internet of Things applications to be represented by a group of software programs. The following software packages are being utilized in this research.

2.2.1 Raspberry Pi Requirements

- **Raspberry Pi OS**

It is the ideal operating system for Raspberry Pi devices, and it is regularly upgraded with an emphasis on reliability and performance; Also, it includes over 35,000 packages [21]. It's worth noting that it's based on the Debian (Linux distribution) and is likewise a free system [22].

- **Python**

Python is a high-level programming language that combines power and clarity [23]. Due to this, it was included in the Raspberry Pi OS operating system since Python is a powerful tool that is easy to learn and use [24]. Version 3.7 is used in this research.

- **TinyDB**

TinyDB is a document-oriented, lightweight database; it’s written entirely in Python and does not require any external resources.

2.2.2 Cloud hosting

Cloud hosting makes software and websites available via cloud resources [25] with minimal start-up costs, resource elasticity, and scale savings [26]. Firebase, a cloud hosting service from Google, is used in this research.

- **Firebase real-time database**

It's a No-SQL, cloud-based database that syncs data in real-time across all clients [27][28].

- **Firebase authentication**

Most applications require user authentication to function properly; a user's identity may allow apps to securely store user data in the cloud and give a consistent, personalized experience across all the user's devices; Firebase Authentication is tightly linked with the rest of the Firebase platform [29][30].

2.2.3 Mobile application

Flutter is used to build a mobile application that is used by the end-user to manage the irrigation process.

- **Flutter**

The Flutter framework from Google allows developers to create natively built, cross-platform mobile apps with a single codebase [31][27]. As a result, the platform-independent emulator can run simultaneously on both Android and iOS devices.

- **Dart**

It is the programming language that is employed to construct applications for Flutter. It was initially created and is now maintained by Google as a JavaScript replacement. Additionally, it adopts a

syntax that is comparable to the Java programming language in an effort to attract Java programmers [32].

3. Results

In this section, the proposed three-layer system architecture, how each layer is implemented, and finally, what the proposed system will look like will be presented as the results of this study.

3.1. System Architecture

The architecture of the proposed smart irrigation system in this study can be described as consisting of three layers: The Internet of Things (IoT) layer, the cloud layer, and the application layer, as shown in Figure 1.

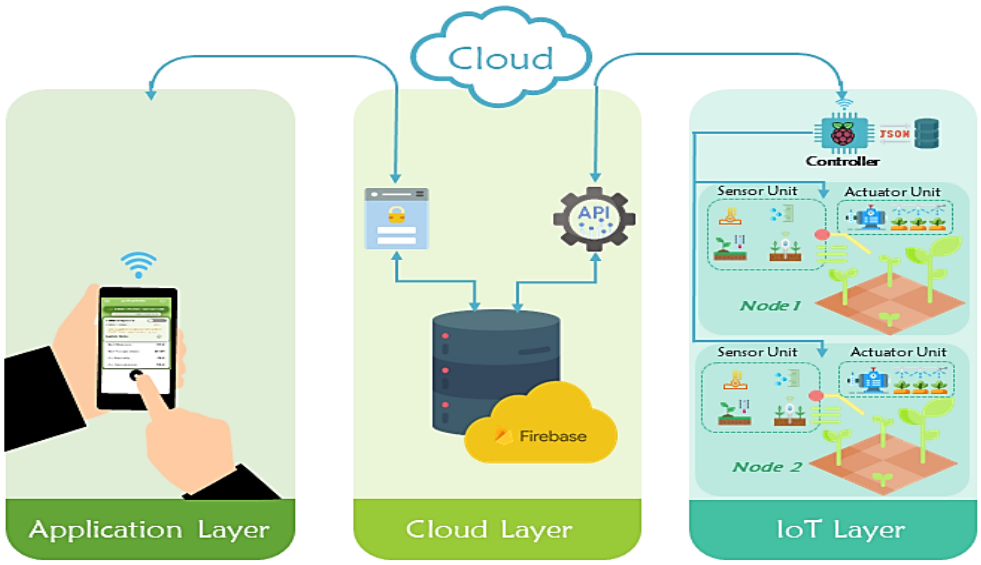

Figure 1. The architecture of the proposed smart irrigation system

3.2. System Implementation

This section describes the implementation of each layer of the proposed system.

3.2.1 IoT layer

The implementation of the IoT layer can be divided into two stages:

I. Hardware implementation stage:

To start the implementation of this stage, a "Pi T-Cobbler Breakout" is used to extend 40 GPIO pins on the "Raspberry Pi Model B" to the breadboard for the purposes of protecting those pins installed on the Raspberry Pi as well as facilitating their handling, that the items (sensors/components) of each node are connected to the GPIO pins.

II. Software implementation stage:

First, "Raspberry OS" is installed on "Raspberry Pi 3 Model B," and then "Visual Studio Code" is installed to start building a "Python 3.7" irrigation management application. Since it's good programming practice to divide enormous code into smaller files for better code management and maintenance, the irrigation control application has been broken into Python modules [33].

The flowchart for this stage can be seen in Figure 2.

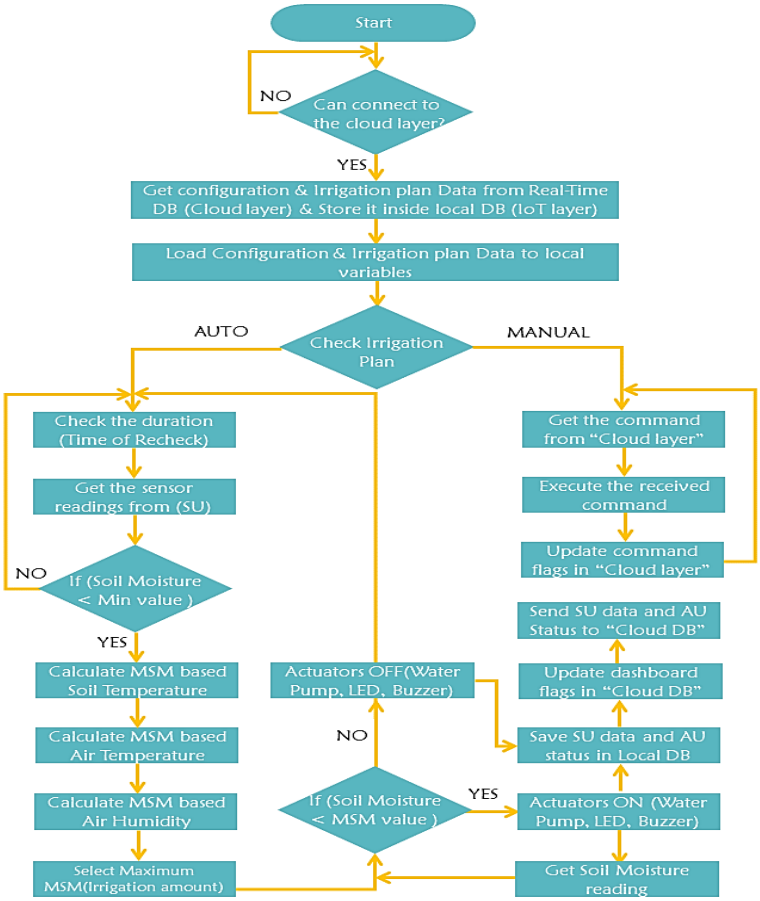

Figure 2. Flowchart of smart irrigation application in "IoT layer."

3.2.2 Cloud layer

Firebase can be used in a mobile app's "application layer" and "IoT layer." These instances enable real-time access to data so updates to the database reach users' devices in real-time. After this instance is generated, it's added to the irrigation management app's "IoT layer" and the mobile app's model. The "application layer" is not directly connected to the cloud layer; instead, the authorized user's e-mail address and password are verified by the verification service before the program is allowed to access the database data.

3.2.3 Application layer

"Android Studio" is used as an (IDE) to create a mobile application that allows the end-user control to the "nodes" of the "IoT layer" across the cloud layer.

3.3. System Demonstration

In this section, each layer of the IoT-based smart irrigation system architecture will be demonstrated after its implementation as follows. The proposed system prototype can be demonstrated in Figure. 3.

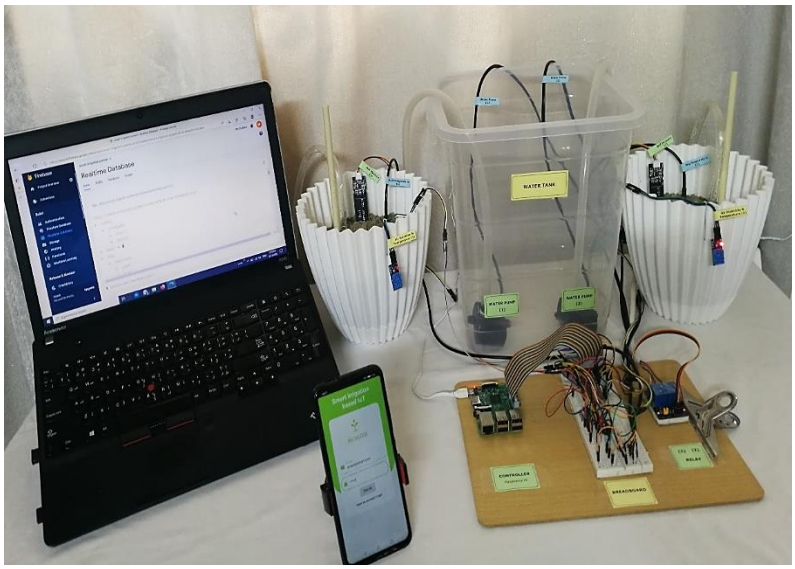

Figure 3. Prototype of the proposed system

3.3.1 IoT layer:

It is shown in Figure 3, the hardware stage in the IoT layer, where the sensors unit (SU) and water pumps were delivered to each node separately so that the decision to irrigate each node is made based on the desired mode (auto/manual) as well as on the sensor values and the appropriate amount of irrigation for each node. On the other hand, the software stage in the IoT layer of the smart irrigation management application when the irrigation mode is automatically selected is demonstrated in Figure 4. A.

In contrast, it is shown in Figure 4. B, the flag state changes after receiving orders such as Pump On/Off or update data.

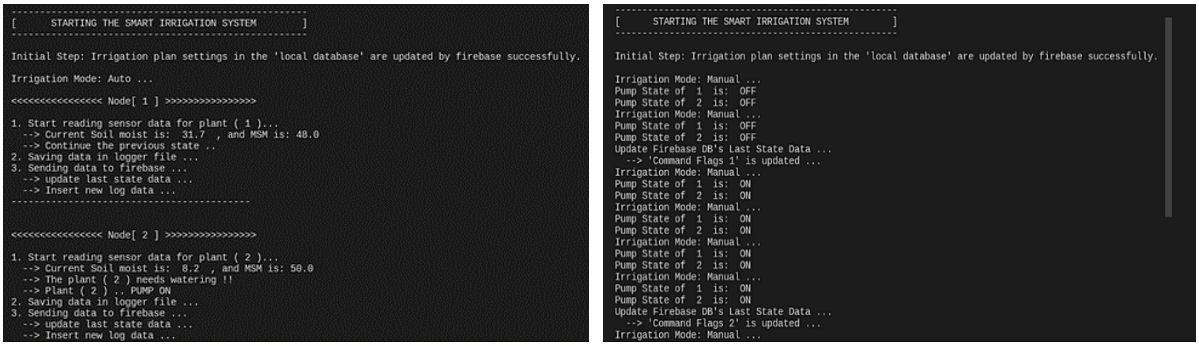

(A) (B)

Figure 4. Smart irrigation management application (IoT layer) (A) Auto irrigation mode. (B) Manual irrigation mode.

3.3.2 Cloud layer:

Figure 5 illustrates how the Firebase real-time database would look after the “Cloud layer” is implemented and connected to the IoT layer and application layer. In addition, if the database data of this layer is updated by the “IoT layer” or the “application layer,” these changes will be indicated by highlighting the changed value.

Figure 5. Firebase real-time database

3.3.3 Application layer:

This layer reflects the actual testing of the proposed system's outputs and their conformity to the objective for which it was built, and it can be clarified using the screens below:

- **Login Screen:**

In this screen, registration data is transferred to Firebase's authentication service in the cloud layer. If the user is authorized to enter, it can access the application or the data stored in the cloud database, which can be used to control and preview IoT data.

- **Main Screen:**

This screen shows after passing the input; from here, the user can select the relevant screen from among the five possible screens: the dashboard screen, the sensors screen, the actuators screen, the settings screen, and the logs screen (Figure 6. A, 6. B, 7).

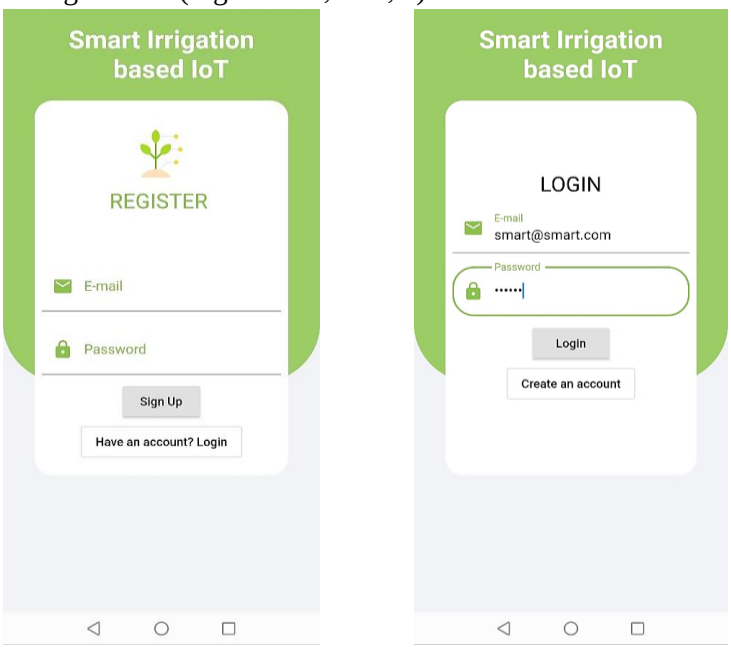

(A) (B)

Figure 6. Login screen (A) Sign up. (B) Login.

Figure 7. Main screen

- **Dashboard Screen:**

This screen displays the soil moisture sensor, soil temperature sensor, ambient temperature and humidity sensor, and water pump status for each node (field/plant) (Figure 8. A). In automated irrigation mode, this page is separated into two areas, one for each node, with the option to see the update time and date (Figure 8. B).

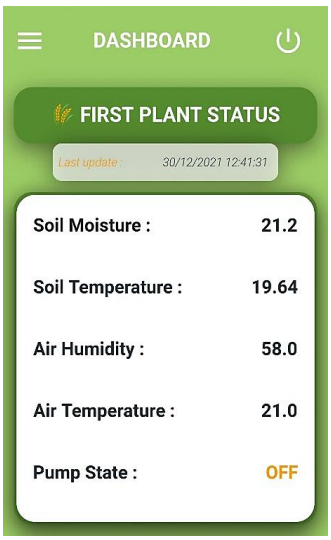

(A)

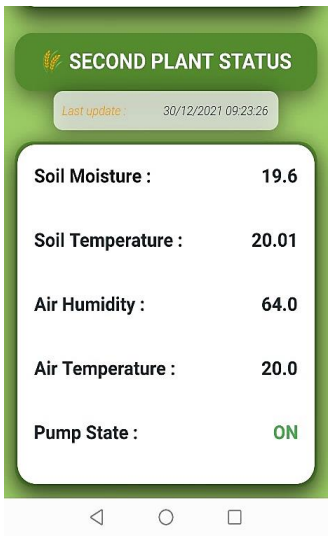

(B)

Figure 8. Dashboard screen (A) The readings of the first plant sensors. (B) The readings of the second plant sensors

- **Sensor's screen:**

This screen displays an end-user the sensor thresholds and ranges. In automatic irrigation mode, the minimum soil moisture sensor reading determines irrigation. It shows the lowest soil moisture or percentage of water in the soil at the point the water pump is operated to irrigate the soil.

The Maximum Soil Moisture (MSM) value influences how much water is needed for soil irrigation. When this value is reached, the soil irrigation pump is turned off.

Figure 9. Sensor's screen (A) Sensor readings. (B) Set the soil moisture value. (C) Set the soil temperature cases.

To achieve dynamism in the irrigation choice, represented by the marginal value, a value can be specified for each plant and adjusted at any moment, as illustrated in Figure 9. B, C shows how the minimum and maximum sensor values can be changed for additional sensors and levels.

- Actuators screen:

Figure 10 shows the irrigation mode screen when each node (field/crop) has its operator (water pump). This screen can be used to manually regulate and update the sensor readings, water pump status, and update time/date. In automatic irrigation mode, the on/off button of the water pump is disabled since the functioning of the pump is controlled automatically.

- **Settings Screen:**

This screen is important for choosing an irrigation plan. The irrigation plan button toggles automatic and manual irrigation. You can also choose the time period during which the sensors are reread to decide if irrigation is needed and how much water to apply. This value can be updated dynamically at any moment (see Figure 11).

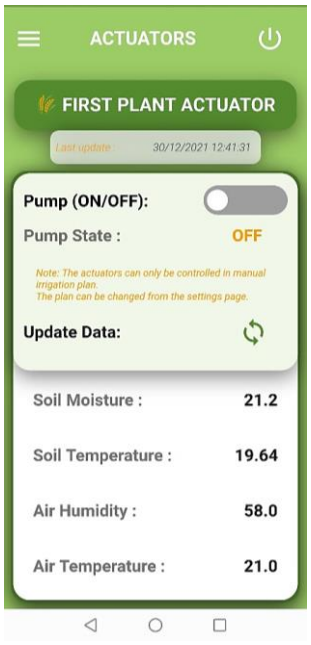

Figure 10. Actuators screen

Figure 11. Settings screen

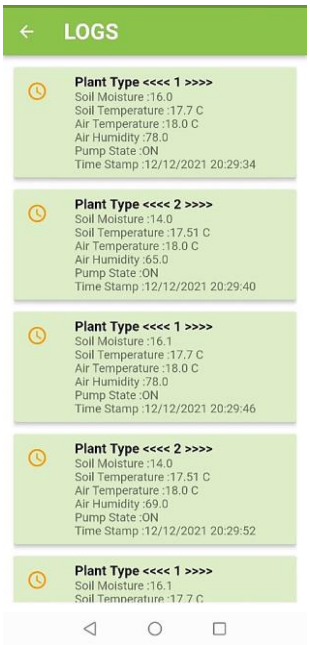

Figure 12. Logs screen

- **Logs Screen:**

This screen displays "Irrigation Need Check for each (Auto) Node" records. Figure 12 shows that the database stores SU values for each node (soil moisture sensor, soil temperature, ambient temperature, and humidity), AU unit or pump status, and the time stamp.

4. Discussion

The literature on smart irrigation using the Internet of Things focuses on answering two main questions: When is an irrigation decision made? How do you determine the appropriate amount of irrigation? Many of the proposed systems have been presented to answer the two previous questions, but they often fall into one of the following problems: (1) Adopting fixed limit values at which the irrigation decision is made, which cannot be changed easily or at any time according to the supervisor. Irrigation process. (2) The amount of irrigation is determined for all crops/plants without taking into account that there is a difference in the amount of water required for each of them, (3) The amount of irrigation is fixed - not dynamic - for one crop/plant without taking into account the difference in other factors affecting the soil such as (soil temperature, air humidity, air temperature) and their influence in determining the appropriate amount based on those variable values.

"Shekhar et al." proposed an intelligent system based on the Internet of Things, which uses only two sensors: one for assessing soil moisture and one for measuring soil temperature. The sensor data is processed by an intelligent algorithm, which predicts the best irrigation decision, but only two sensors were used, and the needs of each individual plant were ignored [34]. An irrigation system that uses the decision tree algorithm has been presented by "Mohammad A. Abbadi et al.," but although this model was developed based on soil characteristics and temperatures, the authors themselves say that because other locations differ from South Jordan Wadi, where the model was developed, the results cannot be generalized to all locations [35]. In addition, in the study of "Rao et al.," an intelligent field monitoring and automation system based on Internet of Things technology has been proposed, which uses two sensors: soil moisture sensors and soil temperature sensors, with bound values chosen to calibrate the sensors based on previous months' values, the irrigation water pump is operated and monitored using a

computer application, However, he neglected to take into account the air temperature and humidity when determining the appropriate amount of irrigation [36].

In this study, a smart system that considers the dynamic factor in determining the appropriate amount of irrigation and the appropriate irrigation time, in addition to other advantages, was proposed to solve the representational issues associated with systems of this type. Practically and for the purpose of applying the algorithm in determining the appropriate amount for irrigation, the following table shows 4 cases for each sensor and its relationship to the soil moisture sensor. It was previously defined for the first plant, depending on either the opinion of experts or the data provided by the competent authorities in agriculture (see Table 1).

Table 1. Settings of the first plant sensors

Sensor	Case No.	Min	Max	MSM
Soil Moisture	----	19	Max(MSM)	----
Soil Temperature	Case 1	<17	17	35
	Case 2	17	36	45
	Case 3	36	64	55
	Case 4	64	>64	65
Air Temperature	Case 1	<10	10	40
	Case 2	10	26	50
	Case 3	26	42	60
	Case 4	42	>42	70
Air Humidity	Case 1	<25	25	65
	Case 2	25	45	55
	Case 3	45	65	45
	Case 4	65	>65	35

Table 2 displays a full day of sensor readings for the first plant. By selecting the correct MSM value for each sensor reading within its related case range, then selecting the maximum value among them, it is possible to determine the proper amount of irrigation to apply when the soil moisture sensor value reaches the minimum value.

Table 2. Read sensors for a full day of the first plant.

Soil Moisture	Soil Temperature	Air Temperature	Air Humidity	Pump State	Time
26.6	5	3.2	82	OFF	03:00
24.9	10	7.3	81	OFF	06:00
23.1	19	15.3	77	OFF	09:00
20.7	24	20.6	73	OFF	12:00
18.5	21	19.2	72	ON	15:00
35.4	16	13.5	75	OFF	18:00
32.5	13	10.7	79	OFF	21:00
29.2	9	5.9	81	OFF	00:00

Figure 13 shows the relationship between the moisture sensor and other sensors, as it is noted that when the reading of the soil moisture sensor reaches a value of 18.5 which is less than the minimum

value at which irrigating must be performed, the system takes an automatic decision to irrigate, as for the amount, after determining the reading of each sensor, we have three values, which are (45, 50, 35), and therefore choose the maximum of which, which is (50).

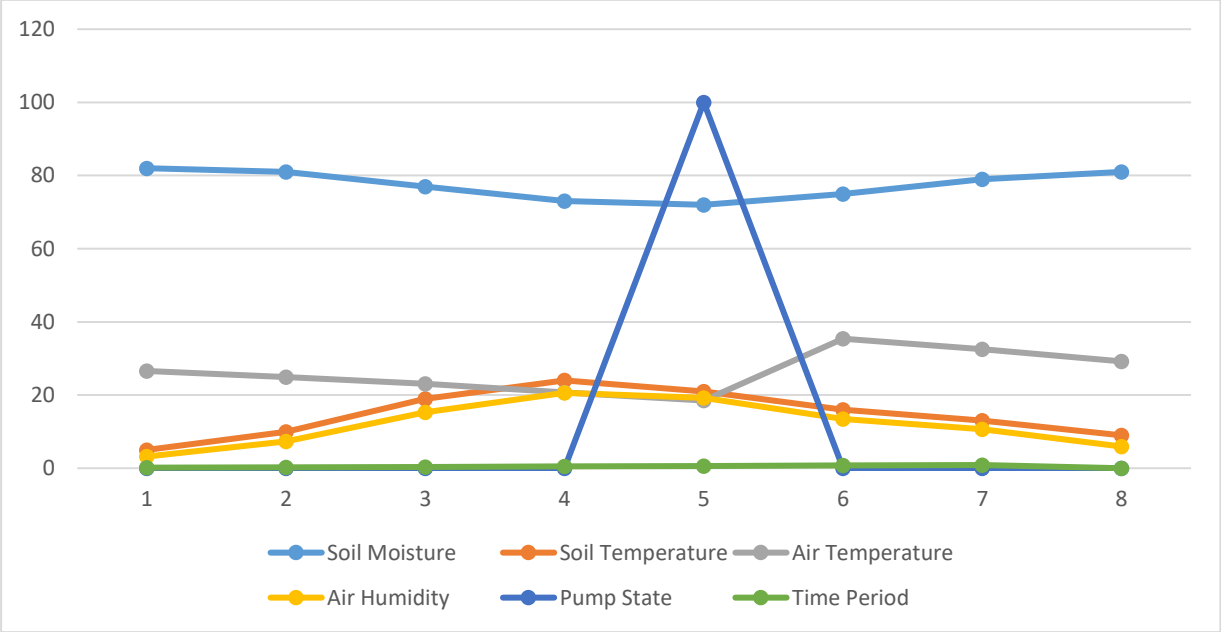

Figure 13. The relationship between reading sensors and determining the appropriate amount of irrigation MSM.

5. Conclusion

The proposed model in this work uses soil moisture, soil temperature, and surrounding temperature and humidity sensors to make irrigation judgments and decide the optimum quantity of irrigation. This study offered various contributions, including adopting a dynamic component in irrigation decision-making, meaning the threshold value is not constant but variable. It may be altered based on plant kind and requirement. The same is true for the appropriate amount of irrigation, which is determined by the relationship between soil temperature, air temperature, humidity, and soil moisture. Based on those values, the value at which soil irrigation will be stopped is chosen, and the watering mode can be manual or automatic.

In the future, it is planned to add rain and water level sensors, as well as an option to select the appropriate irrigation plan based on available quantity, such as basic, medium, or full irrigation, depending on how much water is in the tank and how much is needed. In addition, artificial intelligence and deep learning will be adopted to make irrigation decisions based on data entered into the system during training.

Declaration of Competing Interest

The authors declare no potential conflicts of interest related to the research, authorship, and publication of this article.

Ethical statements

The authors declare that this document does not require ethics committee approval or any special permission. Our study does not cause any harm to the environment and does not involve the use of animal or human subjects.

Authors' Contributions:

W.H.:50%

A.Z.:50%

All authors read and approved the final manuscript

References

[1] "AQUASTAT - FAO's Global Information System on Water and Agriculture," [Online]. Available: https://www.fao.org/aquastat/en/overview/methodology/water-use. [Access Date: 17.01.2022].

[2] L. García, "IoT-based smart irrigation systems: An overview on the recent trends on sensors and IoT systems for irrigation in precision agriculture," *Sensors*, vol. 20, p. 1042, 2020.

[3] J. F. Velasco-Muñoz, "Sustainable irrigation in agriculture: An analysis of global research," *Water*, vol. 11, p. 1758, 2019.

[4] M. Al-HUBAISHI, "SDN INTEGRATION FOR INTERNET OF THINGS," November 2019. [Online]. Available: https://tez.yok.gov.tr/UlusalTezMerkezi/. [Access Date: 23.01.2022].

[5] S. Kechiche, "IoT Connections Forecast: The Rise of Enterprise," 16 December 2019. [Online]. Available: https://data.gsmaintelligence.com/research/research/research-2019/iot-connections-forecast-the-rise-of-enterprise. [Access Date: 23.01.2022].

[6] C. Kamienski, "Smart water management platform: IoT-based precision irrigation for agriculture," *Sensors*, vol. 19, p. 276, 2019.

[7] N. K. Nawandar and V. R. Satpute, "IoT based low cost and intelligent module for smart irrigation system," *Computers and electronics in agriculture*, vol. 162, p. 979–990, 2019.

[8] M. Roopaei, P. Rad and K.-K. R. Choo, "Cloud of things in smart agriculture: Intelligent irrigation monitoring by thermal imaging," *IEEE Cloud computing*, vol. 4, p. 10–15, 2017.

[9] J. Kwok and Y. Sun, "A smart IoT-based irrigation system with automated plant recognition using deep learning," in Proceedings of the 10th international conference on computer modeling and Simulation, 2018.

[10] A. Goap, "An IoT-based smart irrigation management system using Machine learning and open source technologies," *Computers and electronics in agriculture*, vol. 155, p. 41–49, 2018.

[11] O. Friha, "Internet of Things for the Future of Smart Agriculture: A Comprehensive Survey of Emerging Technologies," *IEEE CAA J. Autom. Sinica*, vol. 8, p. 718–752, 2021.

[12] "About us," Raspberry Pi Foundation," [Online]. Available: https://www.raspberrypi.org/about/. [Access Date: 18.01.2022].

[13] L. Upton, "The Raspberry Pi in scientific research," [Online]. Available: https://www.raspberrypi.com/news/the-raspberry-pi-in-scientific-research/. [Access Date: 30.01.2022].

[14] P. Placidi, "Characterization of low-cost capacitive soil moisture sensors for IoT networks," *Sensors*, vol. 20, p. 3585, 2020.

[15] F. S. Muzdrikah, M. S. Nuha and F. A. Rizqi, "Calibration of capacitive soil moisture sensor (sku: Sen0193," in 2018 4th International Conference on Science and Technology (ICST, 2018.

[16] "Programmable Resolution 1-Wire Digital Thermometer (DS18B20) - Datasheet," [Online]. Available: https://datasheets.maximintegrated.com/en/ds/DS18B20.pdf. [Access Date: 30.01.2022].

[17] R. A. Koestoer, "A simple method for calibration of temperature sensor DS18B20 waterproof in oil bath based on Arduino data acquisition system," AIP Conference Proceedings, vol. 2062, 2019.

[18] A. I. Badran and M. Y. Kashmoola, "Smart Agriculture Using Internet of Things: A Survey," in IMDC-SDSP 2020: Proceedings of the 1st International Multi-Disciplinary Conference Theme: Sustainable Development and Smart Planning, IMDC-SDSP 2020, Cyberspace.

[19] "DHT 11 Humidity & Temperature - Datasheet," [Online]. Available: https://www.mouser.com/datasheet/2/758/DHT11-Technical-Data-Sheet-Translated-Version-1143054.pdf. [Access Date: 30.01.2022].

[20] A. Rayes and S. Salam, Internet of Things from hype to reality, Springer, 2017, p. 82–86.

[21] "Raspberry Pi Documentation - Raspberry Pi OS," [Online]. Available: https://www.raspberrypi.com/documentation/computers/os.html#introduction. [Access Date: 01.02.2022].

[22] G. Anand and A. K. Kumawat, "Object detection and position tracking in real time using Raspberry Pi," *Materials Today: Proceedings*, vol. 47, p. 3221–3226, 2021.

[23] "General Python FAQ," [Online]. Available: https://docs.python.org/3/faq/general.html#what-is-python. [Access Date: 01.02.2022].

[24] W. Donat and C. Krause, Learn Raspberry Pi Programming with Python, New York, NY 10013: Apress, 2014.

[25] D. Molnar and S. E. Schechter, "Self Hosting vs. Cloud Hosting: Accounting for the Security Impact of Hosting in the Cloud," WEIS, 2010.

[26] "What is cloud hosting?" [Online]. Available: https://www.ibm.com/cloud/learn/what-is-cloud-hosting. [Access Date: 01.02.2022].

[27] "Firebase Realtime Database | Firebase Documentation," [Online]. Available: https://firebase.google.com/docs/database/. [Access Date: 01.02.2022].

[28] L. Moroney, The firebase realtime database." The Definitive Guide to Firebase, Berkeley, CA: Apress, 2017, p. 51–71.

[29] L. Moroney, Using authentication in firebase." The Definitive Guide to Firebase, Berkeley, CA: Apress, 2017, p. 25–50.

[30] "Firebase Authentication | Firebase Documentation," [Online]. Available: https://firebase.google.com/docs/auth. [Access Date: 01.02.2022].

[31] W. Wu, React Native vs Flutter, Cross-platforms mobile application frameworks, 2018.

[32] G. I. Arb and K. Al-Majdi, "A Freights Status Management System Based on Dart and Flutter Programming Language," *Journal of Physics: Conference Series*, vol. 1530, 2020.

[33] "Modules — Python 3.7.12 documentation," [Online]. Available: https://docs.python.org/3.7/tutorial/modules.html. [Access Date: 07.02.2022].

[34] Y. Shekhar, "Intelligent IoT-based automated irrigation system," *International Journal of Applied Engineering Research*, vol. 12, p. 7306–7320, 2017.

[35] A. H. Blasi, M. A. Abbadi and R. Al-Huweimel, "Machine Learning Approach for an Automatic Irrigation System in Southern Jordan Valley," *Engineering, Technology & Applied Science Research*, vol. 11, p. 6609–6613, 2021.

[36] R. N. Rao and B. Sridhar, "IoT based smart crop-field monitoring and automation irrigation system," in 2018 2nd International Conference on Inventive Systems and Control (ICISC), 2018.